

# Approximation for Cooperative Interactions of a Spatially-Detailed Cardiac Sarcomere Model

TAKUMI WASHIO,<sup>1</sup> JUN-ICHI OKADA,<sup>1</sup> SEIRYO SUGIURA,<sup>2</sup> and TOSHIAKI HISADA<sup>2</sup>

<sup>1</sup>Graduate School of Frontier Sciences, University of Tokyo, 5-1-5, Kashiwanoha, Kashiwa, Chiba 277-0882, Japan; and

<sup>2</sup>Graduate School of Frontier Sciences, University of Tokyo, 7-3-1, Hongo, Bunkyo-ku, Tokyo 113-0033, Japan

(Received 25 October 2011; accepted 15 December 2011; published online 28 December 2011)

Associate Editor Andrew D. McCulloch oversaw the review of this article.

**Abstract**—We developed a novel ordinary differential equation (ODE) model, which produced results that correlated well with the Monte Carlo (MC) simulation when applied to a spatially-detailed model of the cardiac sarcomere. Configuration of the novel ODE model was based on the Ising model of myofilaments, with the “co-operative activation” effect introduced to incorporate nearest-neighbor interactions. First, a set of parameters was estimated using arbitrary Ca transient data to reproduce the combinational probability for the states of three consecutive regulatory units, using single unit probabilities for central and neighboring units in the MC simulation. The parameter set thus obtained enabled the calculation of the state transition of each unit using the ODE model with reference to the neighboring states. The present ODE model not only provided good agreement with the MC simulation results but was also capable of reproducing a wide range of experimental results under both steady-state and dynamic conditions including shortening twitch. The simulation results suggested that the nearest-neighbor interaction is a reasonable approximation of the cooperativity based on end-to-end interactions. Utilizing the modified ODE model resulted in a reduction in computational costs but maintained spatial integrity and co-operative effects, making it a powerful tool in cardiac modeling.

**Keywords**—Cross-bridge, Monte Carlo simulation, Ordinary differential equation (ODE) model, Contraction force, Sarcomere kinetics.

## INTRODUCTION

Mathematical modeling is an indispensable tool in defining the mechanisms of activation and force generation of the cardiac sarcomere. Various mathematical models have been designed to replicate and characterize the cellular processes and activities of

the sarcomere and, recently, detailed structure and filament properties have also been taken into account.<sup>2,4,10,16</sup> However, current models have yet to replicate the anomalously high sensitivity of developed force to changes in the free cytosolic calcium (Ca) concentration, observed under both steady-state and dynamic conditions. This aberrant effect is suggested to be brought about by the “co-operative” interactions among intracellular molecules within the sarcomere. One postulated mechanism of “cooperativity” suggests that the strongly-bound cross-bridge releases the steric hindrance of tropomyosin to facilitate the attachment of nearby cross-bridges. A further potential mechanism underlying the “co-operative” interactions is the end-to-end interactions of regulatory troponin/tropomyosin (T/T) units along the thin filament. In either case, the physical arrangement of each molecular component is suggested to be a critical factor.

To reproduce the “co-operative” effects that occur within the sarcomere, most current models utilize the “phenomenological parameter tuning strategy” to normalize the behavior of cross-bridges and to avoid the necessity of determining the state of each regulatory unit and the interactions among them (mean-field approximation). Although this approach enables the use of ordinary differential equations (ODE), has a lower computational cost, and has been reported to provide a fairly good representation of experimental data,<sup>1,9,13,20,21</sup> the models lack a representation of spatial activity within the cell. This limits the predictive ability of the models and hampers the potential for direct comparisons with experimentally obtained data.<sup>18</sup>

Spatially-distributed models have been proposed that are capable of mimicking the physical arrangement of each functional unit within a cell, including the cross-bridges in the thick and thin filaments of the sarcomere.<sup>8,10,19,22</sup> In these models, the transition rates of each unit are dependent on the states of neighboring

Address correspondence to Takumi Washio, Graduate School of Frontier Sciences, University of Tokyo, 5-1-5, Kashiwanoha, Kashiwa, Chiba 277-0882, Japan. Electronic mail: washio@sml.k.u-tokyo.ac.jp

units and/or the cross-bridge strain to reveal any potential “co-operative” mechanisms that occur. Moreover, the models have been found to have excellent reproducibility. However, the inherent and inevitable problem with this type of model is the necessity of using the computationally expensive Monte Carlo (MC) simulation. Although Rice *et al.*<sup>19</sup> reported an analytical solution to their Ising model of myofilaments without MC simulation, its application is limited to the static state with a simple periodic boundary condition. Very recently, Campbell *et al.*<sup>3</sup> proposed a Markov model approach to represent the states of regulatory units, but the computational costs again limited the number of units studied in the model.

Here we propose a novel method for describing the behavior of a spatially detailed co-operative model using ODE in which the regulatory units are distributed along the sarcomere filament. Through modifications to the Ising model produced by Rice *et al.*,<sup>19</sup> we produced an ODE model that is applicable to a wider range of experimental conditions, including accounting for changes in sarcomere length ( $SL$ ). Our modified ODE model was found to correlate well with the MC simulation over a wide range of dynamically changing Ca concentrations. Moreover, our ODE model is capable of recording the information of neighboring

units and reproducing the co-operative phenomenon arising from molecular interactions along the sarcomere filaments. Importantly, this novel ODE model is associated with greatly reduced computational costs, thereby enabling its application for large scale models of cardiac physiology.

## METHODS

### Description of the Model

The sarcomere model used in the present study is illustrated in Fig. 1. The model consists of a pair of thin filaments (AF) and a single thick filament (MF). Myosin heads (MHs) are arranged symmetrically on the thick filament with regular intervals on both sides of the bare-zone (B-zone). The geometry of the model is summarized in Table 1. To introduce  $SL$  as a factor in the model, we assigned a functional unit to each MH coupled with the opposing segment of thin filament and indexed as “ $i$ ”. This process conflicts somewhat with the traditional practices used in sarcomere modeling where the unit is commonly placed on the thin filament. However, because the helical pitch of the myosin filament is close to that of actin (composed of seven monomeric actins) and regulated by a single

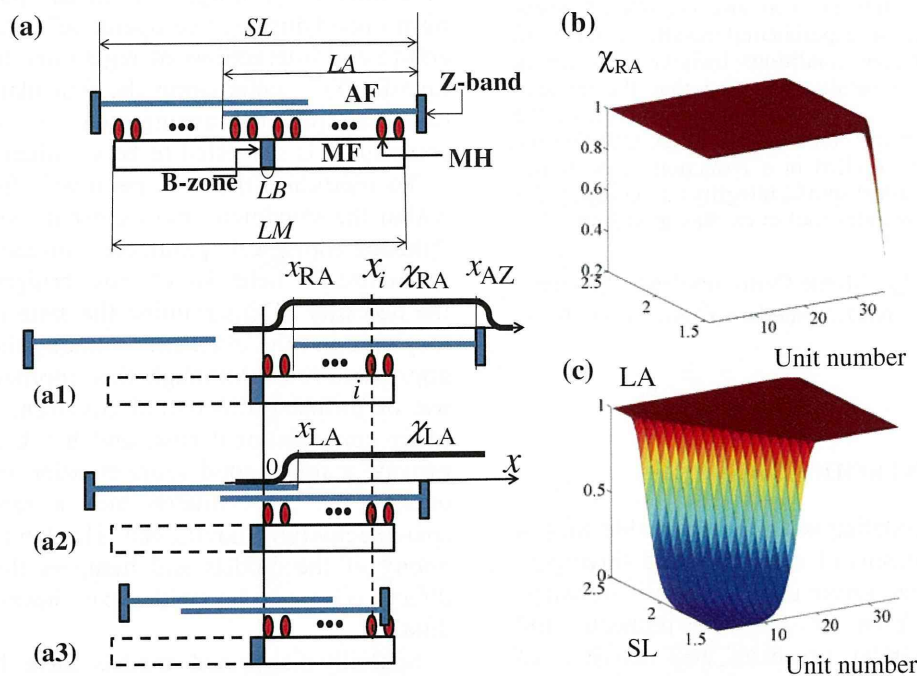


**FIGURE 1.** Schematic of the sarcomere model (a). (a1) Relative position of filaments in the single overlapping state ( $SL > 2LA + LB$ ).  $x_{RA}$ : position of the end of the right thin filament,  $x_{AZ}$ : position of Z-band of the right thin filament,  $x_i$ : position of  $i_{th}$  MH, both measured from the right-hand edge of the bare zone. (a2) The double overlapping state ( $LM < SL < 2LA - LB$ ).  $x_{LA}$ : position of the end of the left thin filament. (a3) State of no overlapping at the MF ends ( $SL < LM$ ). MF: thick filament, MH: myosin head, B-zone: bare zone, AF: thin filament,  $SL$ : sarcomere length  $LA$ : thin filament length,  $LM$ : thick filament length,  $LB$ : bare zone length. Dependence of the lumped parameters  $\chi_{RA}(SL, i)$  (b) and  $\chi_{LA}(SL, i)$  (c) on  $SL$  at individual unit (MH<sub>*i*</sub>).

TABLE 1. Model parameters.

Parameter	Value	Units	
Sarcomere geometry			
LA (length of AF)	1.2	$\mu\text{m}$	*
LM (length of MF)	1.65	$\mu\text{m}$	*
LB (length of B-zone)	0.1	$\mu\text{m}$	*
nu (number of MHs)	36	Unitless	*
Transition rates Ca-bound			
$K_{\text{on}}$	80	$\mu\text{M}^{-1} \text{s}^{-1}$	**
$K_{\text{off}}$	80	$\text{s}^{-1}$	**
$K'_{\text{on}}$	80	$\mu\text{M}^{-1} \text{s}^{-1}$	**
$K'_{\text{off}}$	8	$\text{s}^{-1}$	**
Transition rates N-P			
$Q_0$	3	Unitless	**
$SL_Q$	2.2	$\mu\text{m}$	**
$\alpha_Q$	1.4	$\mu\text{m}^{-1}$	**
$K_{\text{basic}}$	10	$\text{s}^{-1}$	**
$\mu$	10	Unitless	**
$\gamma$	40	Unitless	**
SL dependence			
$a_R$	0.1	$\mu\text{m}$	
$a_L$	0.1	$\mu\text{m}$	
Time interval lengths			
DT (for averaging in MC)	2.5	ms	
$\Delta t$	2.5	$\mu\text{s}$	

Parameter values were adopted \* from Rice *et al.*,<sup>20</sup> \*\* from Rice *et al.*<sup>19</sup> with modifications.

tropinin/tropomyosin (T/T) complex, we believe this strategy is rational. The model was assumed to be symmetrical, and simulation was performed on half of one sarcomere.

The co-operative four-state Markov model proposed by Rice *et al.*<sup>19</sup> was adopted for the present model whereby the state of each functional unit is characterized by the combination of Ca binding (1: bound, 0: not bound) and cross-bridge formation (P: permitted, N: not permitted; Fig. 2). To introduce the co-operative mechanisms occurring in force generation, the factors  $\gamma^n$  and  $\gamma^{-n}$  were multiplied by the transition rates from N to P and from P to N, respectively, where  $n$  ( $=0, 1$  or  $2$ ) is the number of nearest-neighboring MHs in the P-state.

In addition, we modified the following rate constants by multiplying the geometrical factors  $\chi_{\text{RA}}(SL, i)$  and  $\chi_{\text{LA}}(SL, i)$  (Figs. 1A1, A2, 1B and 1C) to introduce a dependence on the filament overlap determined by  $SL$ :

$$\begin{aligned}
 \bar{K}_{\text{np}0}(SL, i) &= \chi_{\text{LA}}(SL, i) \chi_{\text{RA}}(SL, i) K_{\text{np}0}, \\
 \bar{K}_{\text{np}1}(SL, i) &= \chi_{\text{LA}}(SL, i) \chi_{\text{RA}}(SL, i) K_{\text{np}1}, \\
 \bar{K}_{\text{on}}(SL, i) &= \chi_{\text{RA}}(SL, i) K_{\text{on}}, \\
 \bar{K}'_{\text{on}}(SL, i) &= \chi_{\text{RA}}(SL, i) K'_{\text{on}}.
 \end{aligned} \tag{1}$$

The factors  $\chi_{\text{RA}}(SL, i)$  and  $\chi_{\text{LA}}(SL, i)$  were defined for each unit as the function of its position ( $x_i$ ) and the degree of filament overlap, determined by the positions

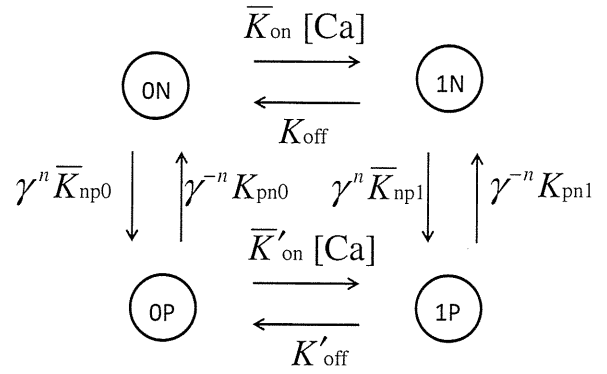


FIGURE 2. The cooperative four-state Markov model. States are coded with the combination of the Ca binding state (0: not bound, 1: bound) and conformation for cross-bridge formation (P: permissive, N: non-permissive). Transitions among the states are governed by the rate constant adjacent to each arrow. To introduce the co-operative behavior for the transition between states P and N, the factors  $\gamma^n$  and  $\gamma^{-n}$  are multiplied by the transition rates from N to P and P to N, respectively, where  $n$  is the number of neighboring MHs in the P-state. The overlines for transition rates  $\bar{K}_{\text{np}0}$ ,  $\bar{K}_{\text{np}1}$ ,  $\bar{K}_{\text{on}}$  and  $\bar{K}'_{\text{on}}$  indicate that these rates are modified according to the  $SL$ .  $[\text{Ca}]$  denotes the free Ca concentration.

of two thin filament ends (the free end ( $x_{\text{RA}}$ ) of the right-hand side filament, the Z-band ( $x_{\text{AZ}}$ ) of the right-hand side filament and the free end ( $x_{\text{LA}}$ ) of the left-hand side filament) (Fig. 1).

$$\begin{aligned}
 x_{\text{AZ}} &= (SL - LB)/2, \quad x_{\text{LA}} = LA - x_{\text{AZ}} - LB, \\
 x_{\text{RA}} &= x_{\text{AZ}} - LA.
 \end{aligned} \tag{2}$$

When there are non-overlapping regions of the two filaments ( $SL > 2LA + LB$ , Fig. 1A1), only the units where  $x_i > x_{\text{RA}}$  can form cross-bridges without the modification to the rate constant. For those cross-bridges located in non-overlapping regions ( $x_i \leq x_{\text{RA}}$ ), the rate constant becomes attenuated as the distance to the MH extends further from the thin filament end:

$$\chi_{\text{RA}}(SL, i) = \begin{cases} \exp\left(- (x_{\text{RA}} - x_i)^2 / a_R^2\right), & x_i \leq x_{\text{RA}} \\ 1, & x_{\text{RA}} < x_i < x_{\text{AZ}}, \\ \exp\left(- (x_i - x_{\text{AZ}})^2 / a_R^2\right), & x_i \geq x_{\text{AZ}} \end{cases} \tag{3}$$

where a step function is smoothed at the ends so that  $\chi_{\text{RA}}$  changes continuously with respect to  $SL$ . The third condition of Eq. (3) becomes effective for determining  $\bar{K}_{\text{np}0}$  and  $\bar{K}_{\text{np}1}$  in Eq. (1) when no overlapping state appears at the right ends of MF (Fig. 1A3). The genesis of the ascending limb in the force-length relation in regions of  $SL$  shorter than the optimal length is a controversial issue. For this model, we assumed that the formation of the cross-bridge was inhibited for



MHs in the double overlap region of the thin filament (Fig. 1A2,  $SL < 2LA - LB$ ):

$$\chi_{LA}(SL, i) = \begin{cases} \exp\left(-\frac{(x_{LA} - x_i)^2}{a_L^2}\right), & x_i \leq x_{LA} \\ 1, & x_i > x_{LA} \end{cases} \quad (4)$$

The parameters  $a_R$  and  $a_L$  determine how rapidly the MHs at the borders of overlapping zone lose their capability to form attached bridges as they become distant from the filament ends. The values were adjusted to agree with the experimental force-length relation and are listed in Table 1. Finally, the MHs at the edges of the filament ( $i = 1$  and  $nu$ ) were assumed to always have N-state neighbors on their null side.

### Monte Carlo Simulation

The MC simulation was performed according to the following rules. For a given random number  $r \in [0, 1]$  generated for each unit ( $i$ th MH) at each time interval ( $[t, t + \Delta t]$ ), the state  ${}^t\alpha_i$  (either 0N, 1N, 0P, or 1P) at time  $t$  transitions to the new state  ${}^{t+\Delta t}\alpha_i = T_{\Delta t}({}^t\alpha_i)$  during the time interval  $[t, t + \Delta t]$  at all MHs as follows:

$$T_{\Delta t}(0N) = \begin{cases} 1N, & 0 \leq r < \Delta t \bar{K}_{on}[Ca] \\ 0P, & \Delta t \bar{K}_{on}[Ca] \leq r < \Delta t (\bar{K}_{on}[Ca] + \gamma^n \bar{K}_{np0}) \\ 0N, & \Delta t (\bar{K}_{on}[Ca] + \gamma^n \bar{K}_{np0}) \leq r \leq 1 \end{cases}$$

$$T_{\Delta t}(1N) = \begin{cases} 0N, & 0 \leq r < \Delta t K_{off} \\ 1P, & \Delta t K_{off} \leq r < \Delta t (K_{off} + \gamma^n \bar{K}_{np1}) \\ 1N, & \Delta t (K_{off} + \gamma^n \bar{K}_{np1}) \leq r \leq 1 \end{cases}$$

$$T_{\Delta t}(1P) = \begin{cases} 1N, & 0 \leq r < \Delta t \gamma^{-n} K_{pn1} \\ 0P, & \Delta t \gamma^{-n} K_{pn1} \leq r < \Delta t (\gamma^{-n} K_{pn1} + K'_{off}) \\ 1P, & \Delta t (\gamma^{-n} K_{pn1} + K'_{off}) \leq r \leq 1 \end{cases}$$

$$T_{\Delta t}(0P) = \begin{cases} 1P, & 0 \leq r < \Delta t K'_{on}[Ca] \\ 0N, & \Delta t \bar{K}'_{on}[Ca] \leq r < \Delta t (\bar{K}'_{on}[Ca] + \gamma^{-n} K_{pn0}) \\ 0P, & \Delta t (\bar{K}'_{on}[Ca] + \gamma^{-n} K_{pn0}) \leq r \leq 1 \end{cases}$$

The time interval  $\Delta t$  was chosen so that none of the values with the coefficient  $\Delta t$  in the third condition of each rule set exceeds 1. The parameter  $n$  is the number of nearest-neighboring MHs ( $i - 1$ th and  $i + 1$ th MHs) in the P-state at time  $t$ .

These transition rate constants were adopted from Rice *et al.*<sup>19</sup> and modified. Some transition rates between the P-state and N-state were calculated with the parameters  $Q$ ,  $K_{basic}$ ,  $\mu$  and  $\gamma$  (Table 1) as follows:

$$K_{np0} = QK_{basic}/\mu, \quad K_{np1} = QK_{basic}, \quad K_{pn0} = K_{basic}\gamma^2, \\ K_{pn1} = K_{basic}\gamma^2, \quad K'_{on} = K_{on}, \quad K'_{off} = K_{off}/\mu. \quad (5)$$

To reproduce the  $SL$  dependence of  $[Ca_{50}]$  on force- $pCa$  relations,<sup>5,14</sup> we introduced the  $SL$  dependence of  $Q$ . We found that the best results were obtained with the  $Q$  value decreasing from  $Q_0 = 3$  linearly with inclination  $\alpha_Q = 1.4 \mu m^{-1}$  as the  $SL$  becomes shorter from  $SL_Q = 2.2 \mu m$ .

$$Q(SL) = \begin{cases} Q_0, & SL \geq SL_Q \\ Q_0 - \alpha_Q(SL_Q - SL), & SL < SL_Q \end{cases} \quad (6)$$

The parameter values are summarized in Table 1.

### Approximation by the ODE Model

There are  $4^{nu}$  combinatory states for the model consisting of  $nu$  regulatory units. First, we introduced a linear ODE that gives the transitions of probability distribution of these combinatory states for a given Ca transient. This ODE provides a probability distribution that correlated well with the previously described MC simulation. However, the direct solution of this ODE is impractical because of the large number of degrees of freedom ( $4^{nu}$  with  $nu = 36$  in our case). Therefore, we introduced a reduced ODE to obtain the averaged probability of the four states at each regulatory unit for the solution of the original ODE.

Each of the four states is represented by four integers:

$$0N \leftrightarrow 1, \quad 1N \leftrightarrow 2, \quad 1P \leftrightarrow 3, \quad 0P \leftrightarrow 4 \quad (7)$$

The probability distribution “P” can then be represented as a linear combination of the  $4^{nu}$  combinatory states:

$$\mathbf{P} = \sum_{1 \leq k_1, \dots, k_{nu} \leq 4} P(k_1, \dots, k_{nu}) \mathbf{e}(k_1, \dots, k_{nu}), \quad (8)$$

The following conditions are fulfilled for the coefficients.

$$\sum_{1 \leq k_1, \dots, k_{nu} \leq 4} P(k_1, \dots, k_{nu}) = 1, \quad P(k_1, \dots, k_{nu}) \geq 0 \quad (9)$$

Here, the basis vector  $\mathbf{e}(k_1, \dots, k_{nu})$  corresponds to the combinatory states of  $nu$  units given in Eq. (7), and  $P(k_1, \dots, k_{nu})$  is interpreted as the probability of the total number of units to take this combinatory state.

The vector space representing probability distributions is composed of  $m = 4^{nu}$  basis vectors. Because we require  $nu = 36$ , the dimension  $m$  becomes so large that a single vector cannot be stored in the memory of a common computer. However, the transition kinetics of the probability distribution can be expressed by a simple linear ODE as follows.

For any given time  $t$ , we define a linear transformation  ${}^t\mathbf{A}$  that represents the transition kinetics at time  $t$  for the combinatory states by giving its action on the basis vectors:



$${}^t\mathbf{A} \cdot \mathbf{e}(k_1, \dots, k_{nu}) = \sum_{1 \leq i \leq nu} \sum_{1 \leq l \leq 4} {}^tA_i(\psi(k_{i-1}), \psi(k_{i+1}))_{l,k_i} \times \mathbf{e}(k_1, \dots, k_{i-1}, l, k_{i+1}, \dots, k_{nu}), \quad (10)$$

where  $\psi$  indicates the N- or P-state by

$$\psi(1) = \text{N}, \psi(2) = \text{N}, \psi(3) = \text{P}, \psi(4) = \text{P}. \quad (11)$$

${}^t\mathbf{A}_i(\xi, \eta)_{l,k}$  is the  $(l,k)$ -component of the  $4 \times 4$  matrix given by

$${}^t\mathbf{A}_i(\xi, \eta) = \begin{bmatrix} -\bar{K}_{\text{on}} {}^t[\text{Ca}] - \gamma^n \bar{K}_{\text{np}0} & K_{\text{off}} & 0 & \gamma^{-n} K_{\text{pn}0} \\ \bar{K}_{\text{on}} {}^t[\text{Ca}] & -K_{\text{off}} - \gamma^n \bar{K}_{\text{np}1} & \gamma^{-n} K_{\text{pn}1} & 0 \\ 0 & \gamma^n \bar{K}_{\text{np}1} & -\gamma^{-n} K_{\text{pn}1} - K_{\text{off}} & \bar{K}_{\text{on}} {}^t[\text{Ca}] \\ \gamma^n \bar{K}_{\text{np}0} & 0 & K_{\text{off}} & -\gamma^{-n} K_{\text{pn}0} - \bar{K}_{\text{on}} {}^t[\text{Ca}] \end{bmatrix}. \quad (12)$$

Here,  $n$  is determined from  $\xi$  and  $\eta$  as the sum of the P-state, the transition rates with the overlines are determined from the position of the  $i$ th MH (as in Eq. 1), and  ${}^t[\text{Ca}]$  is the free Ca concentration at time  $t$ . From the assumption on the boundary, we can assume that  $k_0 = k_{nu+1} = 1$  always holds true in Eq. (10).

It is assumed that the probability distribution  ${}^t\mathbf{P}$  at time  $t$  transposes to the new distribution  ${}^{t+\Delta t}\mathbf{P} = T_{\Delta t}({}^t\mathbf{P})$  at time  $t + \Delta t$ . Using the matrix  ${}^t\mathbf{A}$  defined in Eq. (10),  $T_{\Delta t}(\mathbf{e}(k_1, \dots, k_{nu}))$  (the transition of the specific combinatorial state  $\mathbf{e}(k_1, \dots, k_{nu})$ ) is represented as follows:

$$T_{\Delta t}(\mathbf{e}(k_1, \dots, k_{nu})) = \mathbf{e}(k_1, \dots, k_{nu}) + \Delta t {}^t\mathbf{A} \cdot \mathbf{e}(k_1, \dots, k_{nu}) + O(\Delta t^2). \quad (13)$$

The third term from the right-hand side of Eq. (13) is composed of components with coefficients greater than or equal to the second order of  $\Delta t$ . These components correspond to the states that are different from  $\mathbf{e}(k_1, \dots, k_{nu})$  for more than one unit. Thus, by taking the limit  $\Delta t \rightarrow 0$ , the transition kinetics of the probability distribution  ${}^t\mathbf{P}$  is given by the following linear ODE.

$$\frac{d{}^t\mathbf{P}}{dt} = {}^t\mathbf{A} \cdot {}^t\mathbf{P} \quad (14)$$

From Eqs. (10) and (12), it is apparent that the matrix  ${}^t\mathbf{A}$  has  $2nu$  non-zero off-diagonal entries in each column and row when it is represented as the  $4^{nu} \times 4^{nu}$  matrix on the basis of  $\{\mathbf{e}(k_1, \dots, k_{nu})\}$ . It is also clear that all off-diagonal entries are non-negative and that their sum in each column cancels out exactly with the corresponding diagonal entry. Hence, it can be shown

that the properties in Eq. (9) are preserved if the initial distribution satisfies them.

Let  $\mathbf{D}_i$  and  $\mathbf{D}_i^{\xi, \eta}$  ( $1 \leq i \leq nu$ ,  $\xi, \eta = \text{P or N}$ ) be projections from the combinatorial probability distribution vector space to the four-dimensional vector space defined by

$$\mathbf{D}_i \cdot \mathbf{e}(k_1, \dots, k_i, \dots, k_{nu}) = \mathbf{e}(k_i), \quad (15)$$

and

$$\mathbf{D}_i^{\xi, \eta} \cdot \mathbf{e}(k_1, \dots, k_i, \dots, k_{nu}) = \begin{cases} \mathbf{e}(k_i) & \text{if } \psi(k_{i-1}) = \xi \text{ and } \psi(k_{i+1}) = \eta, \\ \mathbf{0} & \text{otherwise,} \end{cases} \quad (16)$$

where  $\mathbf{e}(k)$ , ( $k = 1, 2, 3, 4$ ) is the  $k$ th unit vector.

Let  ${}^t[\alpha]_i$  denote the state probability that the  $i$ -th MH is in state  $\alpha (= 0\text{N}, 1\text{N}, 0\text{P}, \text{ or } 1\text{P})$  and  ${}^t[\xi, \alpha, \eta]_i$  denote the combinatorial probability that the  $i$ th MH is in state  $\alpha (= 0\text{N}, 1\text{N}, 0\text{P}, \text{ or } 1\text{P})$ , and the right and left neighbors are in state  $\xi$  and  $\eta (= \text{N or P})$ , respectively, at time  $t$ . Thus, with four-dimensional column vectors:

$${}^t\mathbf{p}_i = [{}^t[0\text{N}]_i, {}^t[1\text{N}]_i, {}^t[1\text{P}]_i, {}^t[0\text{P}]_i]^T = \mathbf{D}_i \cdot {}^t\mathbf{P} \quad (17)$$

and

$${}^t\mathbf{p}_i^{\xi, \eta} = [{}^t[\xi, 0\text{N}, \eta]_i, {}^t[\xi, 1\text{N}, \eta]_i, {}^t[\xi, 1\text{P}, \eta]_i, {}^t[\xi, 0\text{P}, \eta]_i]^T = \mathbf{D}_i^{\xi, \eta} \cdot {}^t\mathbf{P}, \quad \xi, \eta = \text{N or P}, \quad (18)$$

The transition kinetics of the  $i$ th MH can be described as follows:

$$\frac{d{}^t\mathbf{p}_i}{dt} = \sum_{\xi, \eta = \text{N, P}} {}^t\mathbf{A}_i(\xi, \eta) \cdot {}^t\mathbf{p}_i^{\xi, \eta}, \quad i = 1, \dots, nu. \quad (19)$$

Understandably, this equation cannot be solved as an ODE because it requires the combinatorial probability  ${}^t[\xi, \alpha, \eta]_i$  at the right-hand side, whereas the variables of the ODE are the state probabilities  ${}^t[\alpha]_i$ . Accordingly, the vector  ${}^t\mathbf{p}_i^{\xi, \eta}$  and its component ( ${}^t[\xi, \alpha, \eta]_i$ ) require approximation using information available from the MC simulation. For this purpose, we focus on the correlation between the combinatorial probability  ${}^t[\xi, \alpha, \eta]_i$  and the state probabilities  ${}^s[\beta]_i$  ( $\beta = 0\text{N}$ ,

1N, 0P, 1P) on the central unit and its neighbors ( $j = i - 1, i, i + 1$ ) for time  $s \leq t$ . Using the data obtained from our MC simulations, it appears that the ratio of the combinatory probability to the central state probability can be accurately approximated as a function of  ${}^t\langle[\mu][\beta][v]\rangle_i$  defined by the following equation with the parameter  $\tau$  representing the memory time length.

$${}^t\langle[\mu][\beta][v]\rangle_i = \frac{1}{\tau} \int_{-\infty}^t \exp\left(-\frac{t-s}{\tau}\right) {}^s[\mu]_{i-1} {}^s[\beta]_i {}^s[v]_{i+1} ds, \quad (20)$$

$\beta, \mu, v = 0N, 1N, 1P \text{ or } 0P$

The memory time length  $\tau$  has a significant influence on the accuracy of the model, thus an optimal value of  $\tau = 66.7$  ms was used for the set of transition rate parameters given in Table 1.

In our ODE model, the function to approximate the combinatory probability is given by:

$$\frac{{}^t[\xi, \alpha, \eta]_i}{{}^t[\alpha]_i} \approx \exp\left(\sum_{\mu, \beta, v=0N, 1N, 1P, 0P} C(i)_{\xi, \alpha, \eta}^{\mu, \beta, v} \langle[\mu][\beta][v]\rangle_i\right). \quad (21)$$

$C(i)_{\xi, \alpha, \eta}^{\mu, \beta, v}$  are parameters determined from the MC simulation results to attain the best approximations (Eq. (21)).  $C(i)_{\xi, \alpha, \eta}^{\mu, \beta, v}$  values were determined by the least square fitting that minimizes the following

$${}^t\mathbf{W}_i(\xi, \eta) = \begin{bmatrix} {}^tW(\xi, 0N, \eta, i) & 0 & 0 & 0 \\ 0 & {}^tW(\xi, 1N, \eta, i) & 0 & 0 \\ 0 & 0 & {}^tW(\xi, 1P, \eta, i) & 0 \\ 0 & 0 & 0 & {}^tW(\xi, 0P, \eta, i) \end{bmatrix}, \quad (24)$$

approximate error  ${}^tR$  over the duration of the MC simulation  $[T_0; T_1]$ .

$${}^tR(\xi, \alpha, \eta, i) = \log \frac{{}^t[\xi, \alpha, \eta]_i}{{}^t[\alpha]_i} - \sum_{\mu, \beta, v=0N, 1N, 1P, 0P} C(i)_{\xi, \alpha, \eta}^{\mu, \beta, v} \langle[\mu][\beta][v]\rangle_i \quad (22)$$

To evaluate the probabilities (the argument of the first term on the right hand side of Eq. (22)), the data obtained from the MC simulations for the duration  $[T_0; T_1]$  was divided into bins of equal time intervals ( $DT = 2.5$  ms) and, in each bin, the number of distinct combinatory states ( $\xi_{i-1}, \alpha_i, \eta_{i+1}$ ) was counted at each time step ( $\Delta t = 2.5$   $\mu$ s) for each individual MH $_i$ .

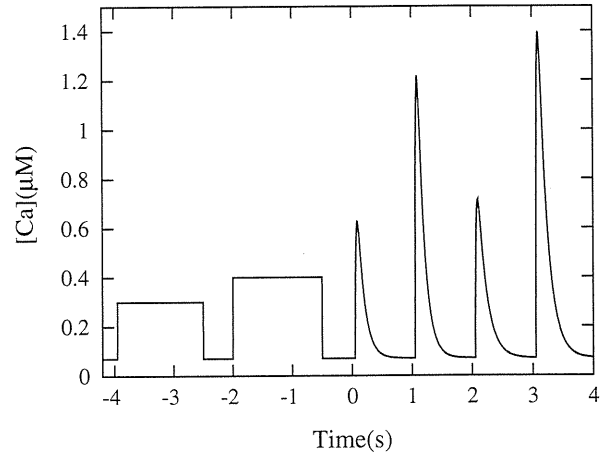


**FIGURE 3.** Ca-transients applied for the determination of ODE parameters. The last four were generated using the equation by Rice *et al.*<sup>20</sup> with the parameter set listed in Appendix.

The MC simulations were performed with various wave forms (Fig. 3) to cover the wide range of conditions.

Once the parameters  $(C(i)_{\xi, \alpha, \eta}^{\mu, \beta, v})$  are determined, ODE simulations can be performed by approximating the combinatory probabilities in Eq. (19) by

$${}^t\mathbf{p}_i^{\xi, \eta} \approx {}^t\mathbf{W}_i(\xi, \eta) \cdot {}^t\mathbf{p}_i \quad (23)$$

with

where the diagonal entries are computed from

$${}^tW(\xi, \alpha, \eta, i) = \exp\left(\min\left(0, \sum_{\mu, \beta, v=0N, 1N, 1P, 0P} C(i)_{\xi, \alpha, \eta}^{\mu, \beta, v} \langle[\mu][\beta][v]\rangle_i\right)\right). \quad (25)$$

Here, the minimum was applied so that  ${}^t[\xi, \alpha, \eta]_i \leq {}^t[\alpha]_i$  is fulfilled in any case. Finally, by substituting  ${}^t\mathbf{p}_i^{\xi, \eta}$  in Eq. (19) with the approximations in Eq. (23), we obtain an ODE:

$$\frac{d^t\mathbf{p}_i}{dt} = \sum_{\xi, \eta=N, P} {}^t\mathbf{A}_i(\xi, \eta) \cdot {}^t\mathbf{W}_i(\xi, \eta) \cdot {}^t\mathbf{p}_i \equiv {}^t\mathbf{B}_i \cdot {}^t\mathbf{p}_i, \quad (26)$$

$i = 1, \dots, nu,$

where the  $4 \times 4$  matrix  ${}^t\mathbf{B}_i$  is given by

$${}^t\mathbf{B}_i = \sum_{\zeta, \eta=N, P} {}^t\mathbf{A}_i(\zeta, \eta) \cdot {}^t\mathbf{W}_i(\zeta, \eta). \quad (27)$$

The validity of this conceptual framework was supported by the excellent predictive power of the ODE model. Although there is no theoretical reason for adopting the exponential function in Eq. (21), we empirically found this style of function enhanced the approximation of temporal rate changes, especially for values close to zero.

Details of the determination and estimation of the ODE parameters are shown in the Appendix.

#### Interpolation of the ODE Parameters for the Simulations of Shortening Contraction

As previously shown, the parameters  $C(i)_{\zeta, \alpha, \eta}^{\mu, \beta, \nu}$  can be estimated for individual MHs at a fixed  $SL$ . For the ODE simulation of shortening contraction where the  $SL$  is continuously changing, we adopted an interpolation method that uses the parameter values obtained at multiple  $SL$ 's  $\{SL_0, SL_1, \dots, SL_{NSL}\}$  with a constant interval  $\Delta SL = SL_k - SL_{k-1}$ . Namely, for any  $SL$  between  $SL_0$  and  $SL_{NSL}$ :

$$C(i)_{\zeta, \alpha, \eta}^{\mu, \beta, \nu} = (1 - \eta)C(SL_{k-1}, i)_{\zeta, \alpha, \eta}^{\mu, \beta, \nu} + \eta C(SL_k, i)_{\zeta, \alpha, \eta}^{\mu, \beta, \nu} \\ \text{for } SL_{k-1} \leq SL \leq SL_k, \quad SL = (1 - \eta)SL_{k-1} + \eta SL_k, \quad (28)$$

In this study,  $\Delta SL = 0.05 \mu\text{m}$  was adopted.

#### Computation

To reduce computational costs, the transition matrices  ${}^t\mathbf{A}_i(\zeta, \eta)$  in Eq. (12) and  ${}^t\mathbf{B}_i$  in Eq. (27) (only for ODE) are updated only at 0.25 ms intervals, whereas the MC states and ODE solutions are updated at 2.5  $\mu\text{s}$  intervals. Such a treatment significantly reduces the computational time for MC and ODE simulations without introducing recognizable error.

The MC and ODE simulation codes were written and executed using Fortran90 on a single core of Intel Xeon X7560 (2.27 GHz). The total number of MHs was 36. Using this previously described protocol, the computation of one sample of the MC simulation took 0.82 s per one second time length. To obtain reasonable mean values, more than a thousand MC samples were required. In contrast, an ODE that used the approximation given in Eqs. (19), (23) and (24) took 0.64 s per one second time length. Thus, the ODE model allowed a great reduction in computational time.

## RESULTS

### Monte Carlo Simulation

In Fig. 4, the results from the MC simulations under steady-state condition are shown for force (in the following text, we use the fraction of bound cross-bridges  $[P](=[0P] + [1P])$  as an index of developed force)– $SL$  relations (Fig. 4a) and  $[P]$ – $p\text{Ca}$  relations (Fig. 4b).  $[P]$ – $p\text{Ca}$  relation clearly demonstrated a significant increase in the maximum  $\text{Ca}^{2+}$ -activated force and increased  $\text{Ca}^{2+}$ -sensitivity (a leftward shift of  $[\text{Ca}_{50}]$ ) at longer  $SL$ s (see also Table 2), which is consistent with previous reports.<sup>5,14</sup> The Hill coefficient decreased a little at short  $SL$ s, but its  $SL$  dependence was much

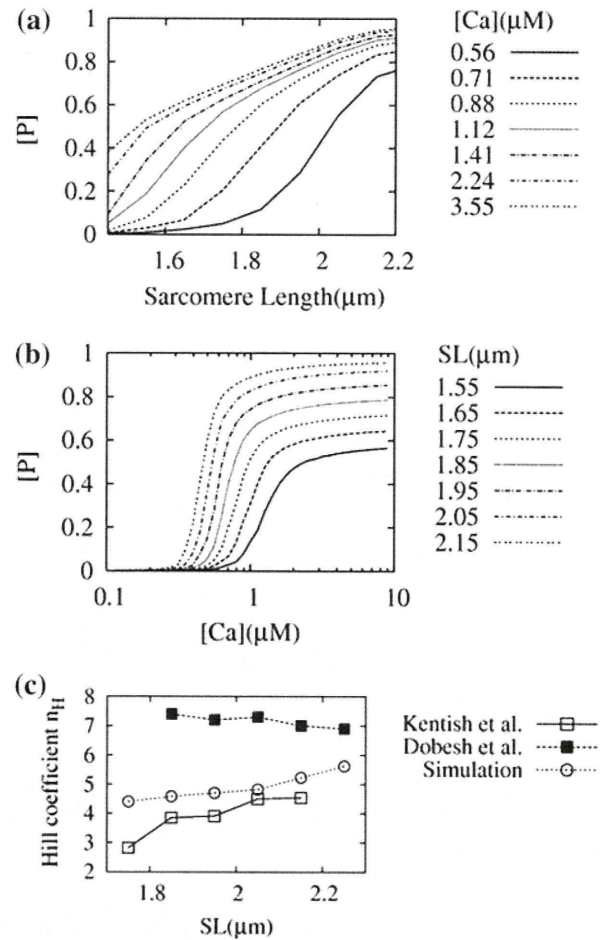


FIGURE 4. Results of MC simulation. Simulation was performed under constant Ca concentration and  $SL$  for 800 s ( $3.2 \times 10^8$  steps). Data from the equilibrium phase (400–800 s) were averaged. The number of the P-state ( $0P + 1P$ ) was assumed as the index of force. (a) Force–length ( $SL$ ) relations shown for different Ca concentrations ranging from 0.56 to 3.55  $\mu\text{M}$ . (b)  $[P]$ – $p\text{Ca}$  relations obtained for different  $SL$ s ranging from 1.45 to 2.15  $\mu\text{m}$ . (c)  $SL$  dependence of the Hill coefficient. Simulation results (closed circle) were compared with the experimental results by Kentish *et al.*<sup>14</sup> (open square) and Dobesh *et al.*<sup>5</sup> (closed square).



smaller than that reported by Kentish *et al.*<sup>14</sup> and closer to the recent results reported by Dobesh *et al.*<sup>5</sup> (Fig. 4c). Data were not available for the shorter range of  $SL$ s in either of these experimental studies.

### Estimates of the ODE Parameters

The estimation of  $\sum C(i)_{\xi, \alpha, \eta}^{\mu, \beta, \nu} \langle [\mu][\beta][\nu] \rangle_i$  in Eq. (22) was performed using the least square results of  $nu = 36$  for each  $SL$ . MC simulation data were obtained from 10,000 samples for the Ca-transient that consists of the six peaks (Fig. 3). The results of this estimation analysis are shown for the units in the middle ( $MH_{18}$ ) and near the filament edge ( $MH_5$ ) at

**TABLE 2. Fitted Hill equation parameters for the MC simulation data.**

$SL$ ( $\mu\text{m}$ )	$[P]_{\text{max}}$	$[Ca_{50}]$ ( $\mu\text{M}$ )	Hill coefficient $n_H$
1.55	0.567	1.40	3.96
1.65	0.645	1.12	4.29
1.75	0.716	0.94	4.40
1.85	0.787	0.81	4.58
1.95	0.856	0.70	4.70
2.05	0.920	0.61	4.82
2.15	0.957	0.53	5.23
2.25	0.967	0.50	5.62

$SL = 2.2 \mu\text{m}$ , in Fig. 5. Comparing the estimated values of  $\left(\sum C(i)_{\xi, \alpha, \eta}^{\mu, \beta, \nu} \langle [\mu][\beta][\nu] \rangle_i\right)$  with the  $\log \left(\langle [\mu][\beta][\nu] \rangle_i\right)$  (Eq. (22)) obtained from the MC simulations, fairly good approximations are attained overall, for all combinations of the indices and the units. However, we found variations that were dependent on the location of the units. For example, observing the unit located in the middle of the filament ( $MF_{18}$ ), the plots for  $\xi, \eta = \text{P, N}$  and  $\xi, \eta = \text{N, P}$  in each of its states (0N, 1N, 1P, and 0P) (middle two rows of Fig. 5a) show similar patterns because of the unit's symmetrical position along the filament, whereas the corresponding plots for the unit near the edge ( $MF_5$ ) (middle two rows of Fig. 5b) show considerable differences. These findings indicate that the present estimation model is capable of capturing heterogeneous trends, which the models with the ring arrangement of the units<sup>3,19</sup> cannot reproduce.

Furthermore, wide variation is found in the values of  $\log \langle W(\xi, \alpha, \eta, i) \rangle$ , supporting the use of a logarithmic scale when the close examination of  $\langle W(\xi, \alpha, \eta, i) \rangle$  is required.

### Comparing the ODE Model and MC Simulation Results

The ODE (Eq. (19)) was simulated using the approximations in Eqs. (23) and (24) to obtain the temporal changes of the fraction of bound cross-bridges

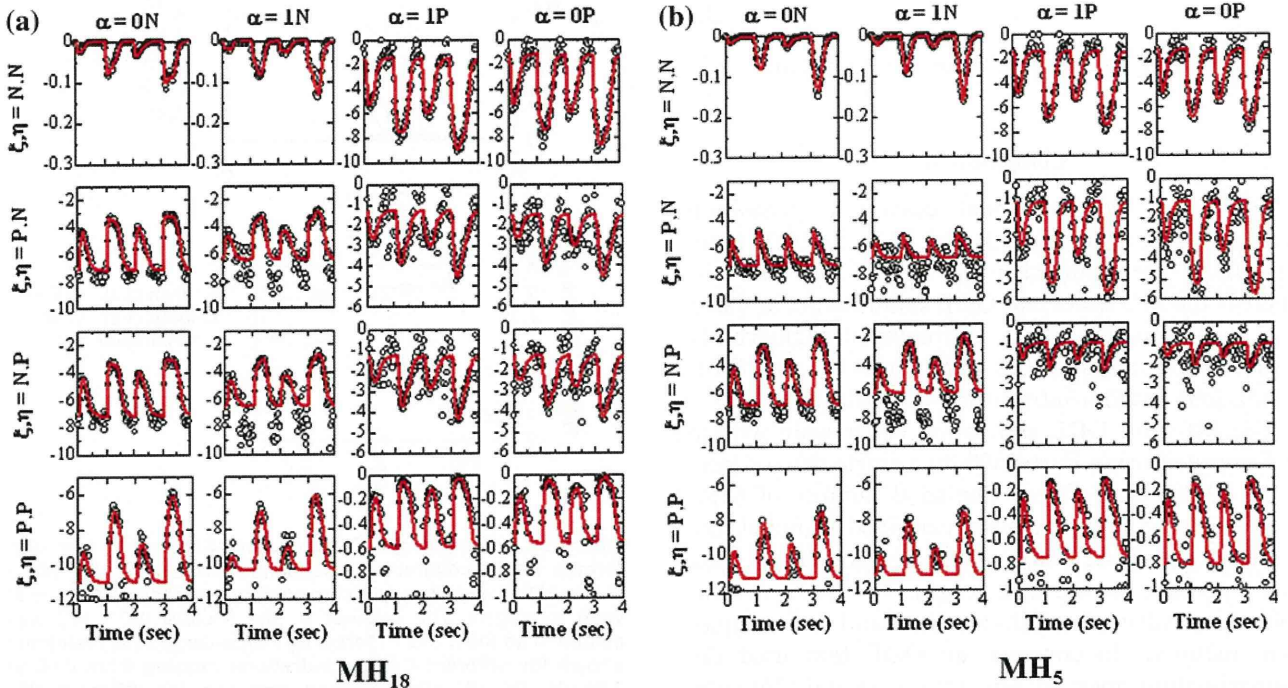


**FIGURE 5.** The least square fitting of the parameters. The values of  $\sum C(i)_{\xi, \alpha, \eta}^{\mu, \beta, \nu} \langle [\mu][\beta][\nu] \rangle_i$  (red lines) estimated from the least square problem of Eq. (6) are compared with  $\log \langle W(\xi, \alpha, \eta, i) \rangle$  (circles), calculated from the MC simulation results using 10,000 samples for various combinations of the MH state ( $\alpha$ , column) and the neighboring states ( $\xi$  and  $\eta$ , row). All results are from the  $MH_{18}$  (the central unit in the filament) in the left panel and from  $MH_5$  (near the left end of MF) in the right panel, respectively, for  $SL = 2.2 \mu\text{m}$ .

[P] in response to the last four Ca peaks in Fig. 3, and the results were compared with those from the MC simulation at different  $SL$ s [ $1.9$  and  $2.2 \mu\text{m}$  (Fig. 6)]. In all MHs at both  $SL$ s, the ODE model and MC simulations correlated well. To clearly demonstrate the agreement, the absolute values of their differences were also shown (ERROR in Fig. 6).

#### Effects of $SL$ on Twitch Duration

Using the same parameter set, we simulated a series of isometric twitches using both the MC simulation and the ODE model while varying the  $SL$  and compared the time courses with the experimental results reported by Janssen *et al.*<sup>12</sup> (Fig. 7). Because the Ca transient was not measured in Janssen's study, we applied the Ca transient shown in the bottom panel, and the force and [P] values were normalized by their peak values at  $SL = 2.2 \mu\text{m}$ . Both the MC simulation (Fig. 7a) and the ODE model (Fig. 7b) reproduced the experimental results reasonably well and clearly showed the  $SL$  dependence of twitch duration.

#### Simulations of Isometric and Shortening Twitches

Next, we applied a Ca transient reported in Janssen and de Tombe<sup>11</sup> to simulate a twitch under both isometric

and shortening contraction (Fig. 8). Again we used the same parameter set, and the force and [P] values were normalized by the respective isometric peak values. For the simulation of a shortening twitch, we applied the time course of  $SL$ , and the interpolated parameter values were used for continuously changing  $SL$ s as described in the methods. Both the MC and ODE simulations successfully reproduced the experimental results ( $R^2 = 0.987$  for MC and  $R^2 = 0.982$  for ODE in the isometric contraction, and  $R^2 = 0.988$  for MC and  $R^2 = 0.977$  for ODE in the shortening contraction), however, to obtain the reasonable agreement, it was necessary to apply the Ca transient recorded under isometric condition to shortening twitch. The reason is not clear, but the use of [P] as the index of force and the absence of mechanisms regulating the affinity of  $\text{Ca}^{2+}$  to troponin C in the model may account for this contradictory result.

#### Effect of Cross-Bridge Kinetics on Force Relaxation

Finally, we examined the effect of cross-bridge kinetics on force relaxation by the MC and ODE simulations. For comparison, we adopted the results reported by Fitzsimons *et al.*<sup>7</sup> in which a stepwise reduction in the  $\text{Ca}^{2+}$  concentration was applied to skinned rat trabeculae composed of either 80%

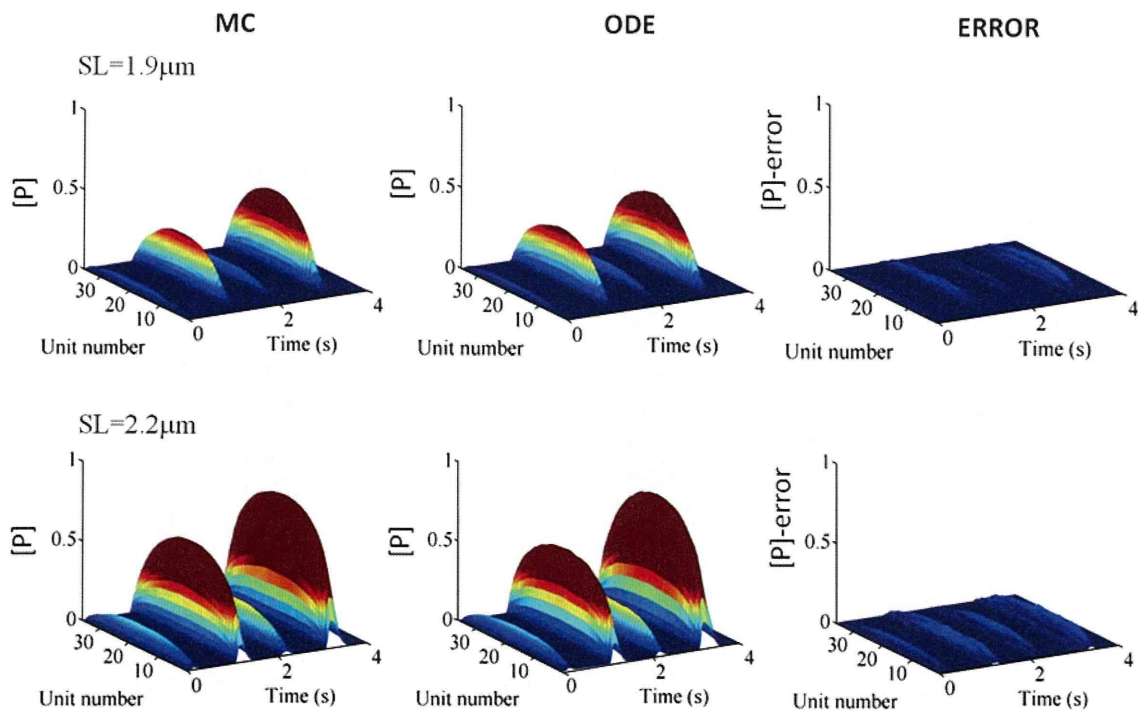
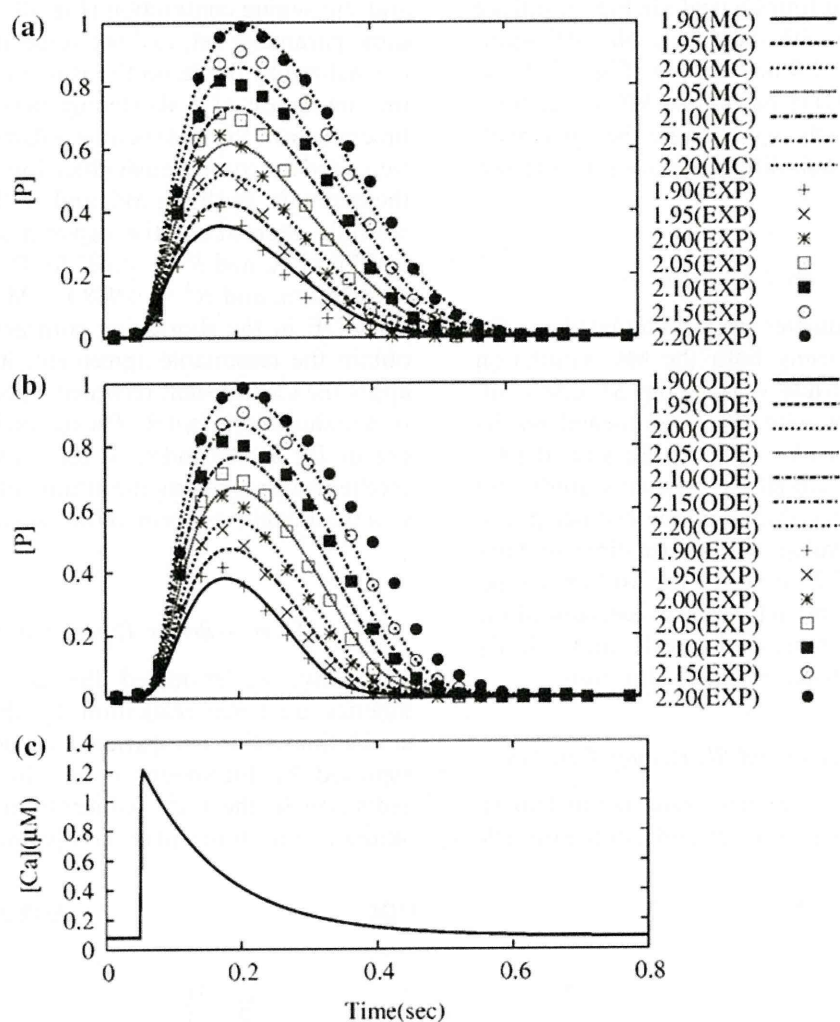


FIGURE 6. Comparisons between the ODE model and MC simulation at individual MHs. The fraction of bound cross-bridges [P] calculated using the ODE model (middle column) are compared with the MC simulation results (left column) while applying the Ca transients in Fig. 3.  $SL$  was set at  $1.9 \mu\text{m}$  (top rows) or  $2.2 \mu\text{m}$  (bottom rows). MC data are displayed as averaged values of 10,000 samples. The absolute values of the differences between the ODE and MC solutions are shown as ERROR (right column). The colors indicate the values (blue:0.0 red:0.3) of ratio (the fraction of bound cross-bridges [P]) (blue:0.0 red:0.3).





**FIGURE 7.** SL dependence of twitch durations. Isometric twitches were compared while varying the SL. (a) Comparisons between the experiment (symbols) and MC simulation (lines); (b) comparisons between the experiment (symbols) and ODE (lines); (c) applied Ca transient.

$\alpha$ -myosin heavy chain (control) or 100%  $\beta$ -myosin heavy chain (hypothyroid). We used the same parameter set for control and reduced the rate constant ( $K_{\text{basic}}$  10 to 3 in Eq. (5)) for the hypothyroid case to replicate the slow cycling rate of a  $\beta$ -myosin heavy chain. To obtain agreement between the MC and ODE simulations ( $R^2 = 0.976$ ), we used a memory length of 250 ms for the hypothyroid case. Both the MC and ODE simulations reproduced the exponential decline in  $[P]$  and the delay in force decline in the hypothyroid preparations that were observed in the experiment (Fig. 9). The half-times for relaxation (control vs. hypothyroid (ms)) were 80 and 152 (MC), and 72 and 117 (ODE) thus comparable to the experimental results (56 and 144) showing a 2-fold increase by hypothyroidism. Normalization of  $[P]$  by the initial value of the MC simulation made the initial ODE value greater than unity because of the differences in the numerical results between the two methods.

## DISCUSSION

In this study, we propose an ODE model of the cardiac sarcomere dynamics with which we can approximate the results of MC simulation performed on the spatially detailed sarcomere model. By this approach, we reduced the huge computational cost usually required for MC simulations. Very recently, Campbell *et al.*<sup>3</sup> developed an ODE model similar to this model that describes nearest neighbor interactions. Their Markov model approach, without using approximation, theoretically gives us the accurate solution of the system, but the use of a ring configuration for the small number of regulatory units cannot reproduce the behavior of the units at the filament ends thus introducing errors. Additionally, the computational costs can become significant as the number of units approaches that of the actual thin filament. Furthermore, the ring simplification does not allow the



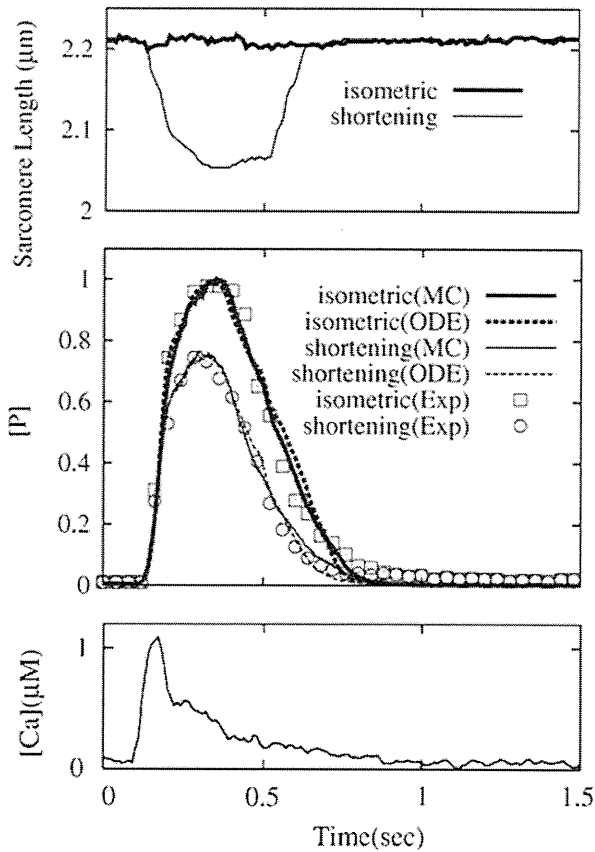


FIGURE 8. Model predictions of twitch contractions in response to experimentally observed Ca transient. Simulations were performed under isometric and shortening conditions. Ca transient (bottom panel) and length change (top panel) were digitized from the study by Janssen *et al.*<sup>11</sup> Calculated force ([P] values) was compared for isometric (case 1) and shortening (case 2) among the MC simulation (solid lines), ODE (dotted lines), and experimental results (symbols). [P] and force were normalized relative to the peak isometric values.

simulation of  $SL$  change during the physiological contraction. Our ODE model with a realistic number of units in linear arrangement demonstrated good correlation with the MC simulation. Moreover, the results from our ODE model indicated that it can be applied to a wide range of cardiac physiology simulations.

#### Spatially-Detailed Sarcomere Model

The framework of the sarcomere model was adopted from the Ising model by Rice *et al.*<sup>19</sup> with modifications. First, to fit the fraction of bound cross-bridges-pCa curves (Fig. 4 upper panel), modulatory factors for Ca binding ( $\chi_{RA}$ ) and cross-bridge formation ( $\chi_{RA} \cdot \chi_{LA}$ ) were multiplied by the transition rates. This modification also aided the reproducibility of the force-length relations.<sup>6,17</sup> Importantly, it was confirmed that in different sets of data, the predictive power of the

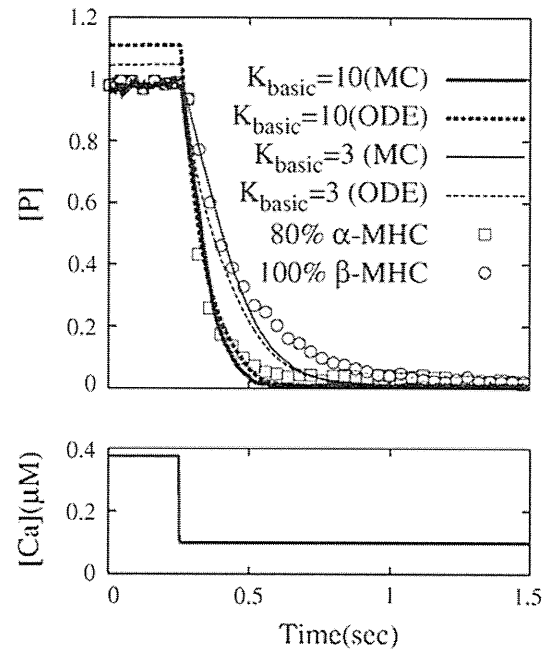


FIGURE 9. The effect of cross-bridge kinetics on the relaxation of force. We simulated experiments by Fitzsimons *et al.*,<sup>7</sup> in which a step reduction in  $Ca^{2+}$  concentration (bottom panel) was applied to the skinned muscle preparations in which myosin isoform composition was either 80%  $\alpha$ -myosin heavy chain or 100%  $\beta$ -myosin heavy chain. Top panel shows the comparison for 80%  $\alpha$  (experiment: square, MC: thick solid line, ODE: thick dotted line) and 100%  $\beta$  (experiment: circle, MC: thin solid line, ODE: thin dotted line).

ODE model is independent of the factors  $\chi_{RA}$  and  $\chi_{LA}$  indicating that the ODE model could accommodate the modifications made to it.

#### Mean Field ODE vs. Spatially-Detailed Models

To avoid the expensive MC simulations required for spatially detailed models of the sarcomere, various ODE models describing the average behavior of the regulatory unit have been reported,<sup>13,15,20,21</sup> but the problems and difficulties in the construction of such a mean field ODE model were pointed out in the literature.<sup>18</sup> Because cooperativity involves the interactions among the spatially arranged molecules, heterogeneous responses of the units are naturally expected and, in fact, the MC simulation studies reported heterogeneous activities of the units during activation.<sup>10,22</sup> Our MC simulation also revealed the heterogeneous activities of the units especially near the edge because these units lacking their neighbors on one side are destined to have small probability for making cross-bridges. The smaller probability of these edge units in turn affects the kinetics of the adjacent units to reduce their probabilities. In this manner, the edge effect is transmitted to the center of the filament, although progressively attenuated, to create the symmetrical

probability distribution as shown in Fig. 6. On the other hand, the probability distribution in this study (Fig. 6) is continuous thus making clear contrast to other spatial MC models, which show discrete “pockets” in probability distributions.<sup>2,10</sup> This difference was originated by our assumption of homogeneous binding probability along the thin filament which ignores the discrete distribution of myosin binding site and differences in their interval (pitch) from that of MHs. With the inclusion of these structural properties, our ODE model will be able to provide detailed information on the activity of each unit and the overall sarcomere without the added computational cost, which an ordinary mean-field approach can never attain.

### Memory Length

In the ODE simulations, we introduced the memory length as the parameter for the estimation of the combinatory probability of the states. As expected from Eq. (20), the memory length should be comparable to the lifetime of each state, which in turn reflects the cycling rate of cross-bridges. In fact, for the simulation of different myosins (Fig. 9), we needed to adjust the memory length. Such an adjustment is needed for myosins with different levels of light chain phosphorylation.

### Application of the Model

We applied our model to the contraction simulation under a wide range of conditions and compared the results with experimental reports. Under steady-state conditions, [P]–pCa relations showed a weak dependence of the Hill coefficient on  $SL$ , which is close to recent data obtained under precise  $SL$  control. In response to the dynamic Ca transients, the model successfully reproduced the  $SL$  dependence of twitch duration under isometric conditions as well. However, the salient feature of the present model is its applicability to the shortening contraction. Although the present application was limited to the case of prescribed length change, the incorporation of a viscoelastic element to the model will enable us to simulate the dynamic experiment with a dynamically changing afterload.

### Limitation

Our ODE approximation method is based on the assumption that the combinatory state probabilities of three consecutive MHs can be represented as functions of the state probabilities of single units, but does not have any firm theoretical basis. Yet, the good predictive power in the simulation tests provides strong support to the validity of the model. However, we cannot be sure whether we can obtain similar results

under other conditions. Further studies are needed. Finally, to evaluate accurately the generated force in heart muscle contraction simulations, we must further introduce viscoelastic effects to the units in P-states.

### Future Directions

The development of an ODE model that approximates a spatially detailed model may open the possibility of the application of such models to a large scale model of circulation, such as the finite element model of the heart. However, the theoretical basis of the present ODE approximation remains to be elucidated.

## APPENDIX

### Determination of the Parameters from MC Simulation Results

The data obtained from the MC simulations of duration  $[T_0:T_1]$  was divided into bins of equal time intervals ( $DT = 2.5$  ms). Because updating in MC simulation was made every  $\Delta t = 2.5 \mu\text{s}$ , each bin was composed of 1000 data sets. In each updating step at each  $MH_i$ , the number of combinational states corresponding to  $(\xi_{i-1}, \alpha_i, \eta_{i+1})$  were counted, where  $\xi_{i-1}, \eta_{i+1} = \text{N or P}$  and  $\alpha_i = \text{0N, 1N, 1P, or 0P}$ . Results were stored in a  $2 \times 4 \times 2 \times nu \times NT$  sized array  $cnt_{16}(\xi_{i-1}, \alpha_i, \eta_{i+1}, i, IT)$  for bin number  $IT = 1, \dots, NT (NT = T/DT)$  by using the following indexing: N = 1, P = 2 and 0N = 1, 1N = 2, 1P = 3, and 0P = 4. The above procedure was performed for the MC simulations repeated over 10,000 times for a single Ca condition (Fig. 3) to fill the array  $cnt_{16}(\xi_{i-1}, \alpha_i, \eta_{i+1}, i, IT)$ . The following arrays ( $cnt_4$  and  $cnt_2$ ) were generated from this data holding the number of individual state of the  $MH_i$  in bin  $IT$ .

$$\begin{aligned} cnt_4(\alpha, i, IT) &= \sum_{\xi, \eta = \text{N, P}} cnt_{16}(\xi, \alpha, \eta, i, IT) \\ cnt_2(\mu, i, IT) &= \begin{cases} cnt_4(0\text{N}, i, IT) + cnt_4(1\text{N}, i, IT), & \text{if } \mu = \text{N} \\ cnt_4(0\text{P}, i, IT) + cnt_4(1\text{P}, i, IT), & \text{if } \mu = \text{P} \end{cases} \end{aligned} \quad (\text{A1})$$

Dividing the elements of these two arrays by the total number of data provides the estimate of probability. Therefore, we can obtain the following ratio that approaches the left-hand side in Eq. (21) as the number of samples increases.

$$W(\xi, \alpha, \eta, i, IT) = \frac{cnt_{16}(\xi, \alpha, \eta, i, IT)}{cnt_4(\alpha, i, IT)} \approx \frac{[ \xi, \alpha, \eta ]_i}{[ \alpha ]_i}, \quad (\text{A2})$$

for  $(IT - 1) \cdot DT \leq t \leq IT \cdot DT$ .

Approximations of  $\langle [\mu][\beta][v] \rangle_i$  can also be obtained from  $cnt_4$  by applying the backward Euler time integration scheme to the ODE:

$$\frac{d}{dt} \langle [\mu][\beta][v] \rangle_i + \frac{1}{\tau} \langle [\mu][\beta][v] \rangle_i = \frac{1}{\tau} \langle [\mu]_i' [\beta]_i' [v]_i' \rangle, T_0 < t \leq T_1 \quad (\text{A3})$$

that is fulfilled by  $\langle [\mu][\beta][v] \rangle_i$  in Eq. (20) in the main text. This results in the following:

$$\begin{aligned} {}^{IT+1} \langle [\mu][\beta][v] \rangle &= \frac{1}{DT + \tau} \left( \tau \cdot {}^{IT} \langle [\mu][\beta][v] \rangle \right. \\ &\quad \left. + DT \cdot \frac{mcnt(\mu, \beta, v, i, IT)}{(DT/\Delta t)^3 \cdot MT^3} \right) \end{aligned} \quad (\text{A4})$$

$$\begin{aligned} \text{with } mcnt(\mu, \beta, v, i, IT) &= cnt_4(\mu, i, IT) cnt_4 \\ &\quad \times (\beta, i, IT) cnt_4(v, i, IT). \end{aligned} \quad (\text{A4})$$

Here,  $MT$  is the repeat number of MC simulations, and the interval index  $IT$  is identified with time  $t = IT \cdot DT - T_0$ .

The parameters  $C(i)_{\xi, \alpha, \eta}^{\mu, \beta, v}$  were determined by minimizing the residual  $R$  in its logarithmic form as:

$$\begin{aligned} R(\xi, \alpha, \eta, i, IT) &= \log W(\xi, \alpha, \eta, i, IT) \\ &\quad - \sum_{\mu, \beta, v=0N, 1N, 1P, 0P} C(i)_{\xi, \alpha, \eta}^{\mu, \beta, v} {}^{IT} \langle [\mu][\beta][v] \rangle. \end{aligned} \quad (\text{A5})$$

right-hand side of Eq. (A6) was added to avoid extraordinarily large values for the parameters  $C(i)_{\xi, \alpha, \eta}^{\mu, \beta, v}$ . In our simulations,  $\varepsilon = 10^{-5}$  and  $\bar{C} = -10$  were adopted.

The least square problem for the error  $E$  in Eq. (A6) results in the following system of linear equations with 64 unknowns  $C(i)_{\xi, \alpha, \eta}^{\bar{\mu}, \bar{\beta}, \bar{v}}$  ( $\bar{\mu}, \bar{\beta}, \bar{v} = 0N, 1N, 1P, 0P$ ).

$$\begin{aligned} \sum_{\bar{\mu}, \bar{\beta}, \bar{v}} \left( a_{\mu, \beta, v}^{\bar{\mu}, \bar{\beta}, \bar{v}} + \varepsilon \delta_{\mu, \beta, v}^{\bar{\mu}, \bar{\beta}, \bar{v}} \right) C(i)_{\xi, \alpha, \eta}^{\bar{\mu}, \bar{\beta}, \bar{v}} &= b_{\mu, \beta, v}, \\ \mu, \beta, v &= 0N, 1N, 1P \text{ or } 0P \end{aligned} \quad (\text{A7})$$

Here, the coefficients in Eq. (A7) are given by

$$\begin{aligned} a_{\mu, \beta, v}^{\bar{\mu}, \bar{\beta}, \bar{v}} &= \sum_{IT=1}^{NT} \frac{cnt_{16}(\xi, \alpha, \eta, i, IT)}{MT} {}^{IT} \langle [\mu][\beta][v] \rangle {}^{IT} \langle [\bar{\mu}][\bar{\beta}][\bar{v}] \rangle + \varepsilon, \\ b_{\mu, \beta, v} &= \sum_{IT=1}^{NT} \frac{cnt_{16}(\xi, \alpha, \eta, i, IT)}{MT} {}^{IT} \langle [\mu][\beta][v] \rangle \\ &\quad \times \log W(\xi, \alpha, \eta, i, IT) - \varepsilon \left( C(i)_{\xi, \alpha, \eta}^{\mu, \beta, v} - \bar{C} \right), \\ \delta_{\mu, \beta, v}^{\bar{\mu}, \bar{\beta}, \bar{v}} &= \begin{cases} 1, & \text{if } \bar{\mu} = \mu, \bar{\beta} = \beta, \bar{v} = v, \\ 0, & \text{otherwise.} \end{cases} \end{aligned} \quad (\text{A8})$$

#### Generation of test Ca transients

The last 4 Ca transients in Fig. 3 were generated by the following equation proposed by Rice *et al.*,<sup>20</sup> with the parameter set listed below.

$$[Ca](t) = \begin{cases} Ca_{\text{diastolic}} \\ \left( \frac{Ca_{\text{amplitude}} - Ca_{\text{diastolic}}}{\beta} \right) \times \left( \exp\left(-\frac{t-t_{\text{start}}}{\tau_1}\right) - \exp\left(\frac{t-t_{\text{start}}}{\tau_2}\right) \right) + Ca_{\text{diastolic}} \end{cases} \quad (\text{A9})$$

In practice, we solved the following least-square problem for errors with weights of bias ( $cnt_{16}$ ) on the  $\log W$  values derived from the larger number of samples assuming their reliability.

$$\begin{aligned} E(\xi, \alpha, \eta, i) &= \sum_{IT=1}^{NT} \frac{cnt_{16}(\xi, \alpha, \eta, i, IT)}{MT} R(\xi, \alpha, \eta, i, IT)^2 \\ &\quad + \varepsilon \sum_{\mu, \beta, v} \left( C(i)_{\xi, \alpha, \eta}^{\mu, \beta, v} - \bar{C} \right)^2 \end{aligned} \quad (\text{A6})$$

Through this procedure,  $W = 0$  is naturally eliminated in the error evaluation. The second term on the

with

$$\beta = \left( \frac{\tau_1}{\tau_2} \right)^{-1/\left(\frac{\tau_1}{\tau_2}-1\right)} - \left( \frac{\tau_1}{\tau_2} \right)^{-1/\left(\frac{\tau_2}{\tau_1}-1\right)}. \quad (\text{A10})$$

1st:  $t_{\text{start}} = 0.05$  s,  $Ca_{\text{diastolic}} = 0.07$   $\mu\text{M}$ ,

$Ca_{\text{amplitude}} = 1.4$   $\mu\text{M}$ ,  $\tau_1 = 0.02$  s,  $\tau_2 = 0.11$  s

2nd:  $t_{\text{start}} = 1.05$  s,  $Ca_{\text{diastolic}} = 0.07$   $\mu\text{M}$ ,

$Ca_{\text{amplitude}} = 2.8$   $\mu\text{M}$ ,  $\tau_1 = 0.02$  s,  $\tau_2 = 0.11$  s



3rd:  $t_{\text{start}} = 2.05 \text{ s}$ ,  $\text{Ca}_{\text{diastolic}} = 0.07 \mu\text{M}$ ,  
 $\text{Ca}_{\text{amplitude}} = 1.4 \mu\text{M}$ ,  $\tau_1 = 0.02 \text{ s}$ ,  $\tau_2 = 0.14 \text{ s}$

4th:  $t_{\text{start}} = 3.05 \text{ s}$ ,  $\text{Ca}_{\text{diastolic}} = 0.07 \mu\text{M}$ ,  
 $\text{Ca}_{\text{amplitude}} = 2.8 \mu\text{M}$ ,  $\tau_1 = 0.02 \text{ s}$ ,  $\tau_2 = 0.14 \text{ s}$

### ACKNOWLEDGMENTS

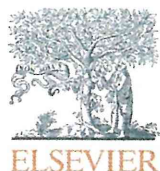
This study was supported by the Japan Science and Technology Agency under the grant Collaborative Development of Innovative Seeds-Practicability Verification Stage, and the Japan Society for the Promotion of Science (JSPS) through its “Funding Program for World-Leading Innovative R&D on Science and Technology (FIRST Program).”

### OPEN ACCESS

This article is distributed under the terms of the Creative Commons Attribution Noncommercial License which permits any noncommercial use, distribution, and reproduction in any medium, provided the original author(s) and source are credited.

### REFERENCES

- <sup>1</sup>Campbell, K. Rate constant of muscle force redevelopment reflects cooperative activation as well as cross-bridge kinetics. *Biophys. J.* 72:254–262, 1997.
- <sup>2</sup>Campbell, K. S. Filament compliance effects can explain tension overshoots during force development. *Biophys. J.* 91:4102–4109, 2006.
- <sup>3</sup>Campbell, S. G., F. V. Lionetti, K. S. Campbell, and A. D. McCulloch. Coupling of adjacent tropomyosins enhances cross-bridge-mediated cooperative activation in a Markov model of the cardiac thin filament. *Biophys. J.* 98:2254–2264, 2010.
- <sup>4</sup>Daniel, T. L., A. C. Trimble, and P. B. Chase. Compliant realignment of binding sites in muscle: transient behavior and mechanical tuning. *Biophys. J.* 74:1611–1621, 1998.
- <sup>5</sup>Dobesh, D. P., J. P. Konhilas, and P. P. de Tombe. Cooperative activation in cardiac muscle: impact of sarcomere length. *Am. J. Physiol. Heart Circ. Physiol.* 282: H1055–H1062, 2002.
- <sup>6</sup>Edman, K. A. Contractile properties of mouse single muscle fibers, a comparison with amphibian muscle fibers. *J. Exp. Biol.* 208:1905–1913, 2005.
- <sup>7</sup>Fitzsimons, D. P., J. R. Patel, and R. L. Moss. Role of myosin heavy chain composition in kinetics of force development and relaxation in rat myocardium. *J. Physiol.* 15:171–183, 1998.
- <sup>8</sup>Geeves, M., H. Griffiths, S. Mijailovich, and D. Smith. Cooperative  $[\text{Ca}^{2+}]$ -dependent regulation of the rate of myosin binding to actin: solution data and the tropomyosin chain model. *Biophys. J.* 100:2679–2687, 2011.
- <sup>9</sup>Hunter, P. J., A. D. McCulloch, and H. E. D. J. ter Keurs. Modeling the mechanical properties of cardiac muscle. *Prog. Biophys. Mol. Biol.* 69:289–331, 1998.
- <sup>10</sup>Hussan, J., P. P. de Tombe, and J. J. Rice. A spatially detailed myofilament model as a basis for large-scale biological simulations. *IBM J. Res. Dev.* 50:583–600, 2006.
- <sup>11</sup>Janssen, P. M., and P. P. de Tombe. Uncontrolled sarcomere shortening increases intracellular  $\text{Ca}^{2+}$  transient in rat cardiac trabeculae. *Am. J. Physiol.* 272:H1892–H1897, 1997.
- <sup>12</sup>Janssen, P. M., and W. C. Hunter. Force, not sarcomere length, correlates with prolongation of isosarcometric contraction. *Am. J. Physiol.* 269:H676–H685, 1995.
- <sup>13</sup>Katsnelson, L. B., T. B. Sulman, O. E. Solovyova, and V. S. Markhasin. Cooperative mechanisms of thin filament activation and their contribution to the myocardial contractile function: assessment in a mathematical model. *Biophysics* 54:39–46, 2009.
- <sup>14</sup>Kentish, J. C., H. E. D. J. ter Keurs, L. Ricciardi, J. J. J. Bucx, and M. I. M. Noble. Comparison between the sarcomere length–force relations of intact and skinned trabeculae from rat right ventricle: influence of calcium concentrations on these relations. *Circ. Res.* 58:755–768, 1986.
- <sup>15</sup>Landesberg, A., and S. Sideman. Mechanical regulation of cardiac muscle by coupling calcium kinetics with cross-bridge cycling. *Am. J. Physiol.* 267:H779–H795, 1994.
- <sup>16</sup>Mijailovich, S. M., J. J. Fredberg, and J. P. Butler. On the theory of muscle contraction: filament extensibility and the development of isometric force and stiffness. *Biophys. J.* 71:1475–1484, 1996.
- <sup>17</sup>Rassier, D. E., B. R. Macintosh, and W. Herzog. Length dependence of active force production in skeletal muscle. *J. Appl. Physiol.* 86:1445–1457, 1999.
- <sup>18</sup>Rice, J. J., and P. P. de Tombe. Approaches to modeling cross-bridges and calcium-dependent activation in cardiac muscle. *Prog. Biophys. Mol. Biol.* 85:179–195, 2004.
- <sup>19</sup>Rice, J. J., G. Stolovitzky, Y. Tu, and P. P. de Tombe. Ising model of cardiac thin filament activation with nearest-neighbor cooperative interactions. *Biophys. J.* 84:897–909, 2003.
- <sup>20</sup>Rice, J. J., F. Wang, D. M. Bers, and P. P. de Tombe. Approximate model of cooperative activation and cross-bridge cycling in cardiac muscle using ordinary differential equations. *Biophys. J.* 95:2368–2390, 2008.
- <sup>21</sup>Rice, J. J., R. L. Winslow, and W. C. Hunter. Comparison of putative cooperative mechanisms in cardiac muscle: length dependence and dynamic responses. *Am. J. Physiol. Heart Circ. Physiol.* 276:1734–1754, 1999.
- <sup>22</sup>Zou, G., and G. N. Phillips, Jr. A cellular automaton model for the regulatory behavior of muscle thin filaments. *Biophys. J.* 67:11–28, 1994.



## Critical role of cardiac t-tubule system for the maintenance of contractile function revealed by a 3D integrated model of cardiomyocytes

Asuka Hatano, Jun-ichi Okada, Toshiaki Hisada, Seiryu Sugiura\*

Graduate School of Frontier Sciences, The University of Tokyo, 5-1-5 Kashiwanoha, Kashiwa, Chiba 277-8581, Japan

### ARTICLE INFO

#### Article history:

Accepted 30 September 2011

#### Keywords:

Excitation–contraction coupling  
Subcellular structure  
t-tubule  
Reaction–diffusion  
Finite element methods

### ABSTRACT

T-tubules in mammalian ventricular myocytes constitute an elaborate system for coupling membrane depolarization with intracellular  $Ca^{2+}$  signaling to control cardiac contraction. Deletion of t-tubules (detubulation) has been reported in heart diseases, although the complex nature of the cardiac excitation–contraction (E–C) coupling process makes it difficult to experimentally establish causal relationships between detubulation and cardiac dysfunction. Alternatively, numerical simulations incorporating the t-tubule system have been proposed to elucidate its functional role. However, the majority of models treat the subcellular spaces as lumped compartments, and are thus unable to dissect the impact of morphological changes in t-tubules. We developed a 3D finite element model of cardiomyocytes in which subcellular components including t-tubules, myofibrils, sarcoplasmic reticulum, and mitochondria were modeled and realistically arranged. Based on this framework, physiological E–C coupling was simulated by simultaneously solving the reaction–diffusion equation and the mechanical equilibrium for the mathematical models of electrophysiology and contraction distributed among these subcellular components. We then examined the effect of detubulation in this model by comparing with and without the t-tubule system. This model reproduced the  $Ca^{2+}$  transients and contraction observed in experimental studies, including the response to beta-adrenergic stimulation, and provided detailed information beyond the limits of experimental approaches. In particular, the analysis of sarcomere dynamics revealed that the asynchronous contraction caused by a large detubulated region can lead to impairment of myocyte contractile efficiency. These data clearly demonstrate the importance of the t-tubule system for the maintenance of contractile function.

© 2011 Elsevier Ltd. All rights reserved.

### 1. Introduction

In mammalian ventricular myocytes, the cell membrane (sarcolemma) invaginates to the cell interior at a regular interval to form the well-organized transverse (t-) tubule system. As voltage-operated L-type  $Ca^{2+}$ -channels are clustered in the t-tubules where they face the junctional part of the sarcoplasmic reticulum (SR) in close proximity, the t-tubule system is believed to play a crucial role in coupling the depolarization signal with  $Ca^{2+}$ -release from the SR (Brette and Orchard, 2003). In fact, atrial myocytes with a poorly-developed t-tubule system exhibit slow propagation of the  $Ca^{2+}$  signal from the periphery to the center of the cell (Kirk et al., 2003). Further, experimental deletion of t-tubules (detubulation) in ventricular myocytes by osmotic expansion (Brette et al., 2002; Kawai et al., 1999) or long term culture (Louch et al., 2004) results in an asynchronous rise in intracellular  $Ca^{2+}$  concentration [ $Ca^{2+}$ ] upon electrical

stimulation as in pathological deletion (Dibb et al., 2009; Heinzel et al., 2008). Nevertheless, the causal relationship between t-tubule structure, [ $Ca^{2+}$ ] dyssynchrony, and contractile dysfunction of the myocytes often observed in diseased hearts remains unclear. For instance, structural remodeling of the t-tubule system is not only observed in the advanced stage of heart failure (Song et al., 2006), but it can occasionally start early in the compensated stage of hypertrophied hearts without contractile dysfunction (Wei et al., 2010). Remodeling includes the t-tubular disarray observed in mechanically unloaded myocytes, in which abnormal  $Ca^{2+}$  release is observed without appreciable changes in action potential and density of t-tubules as estimated from membrane fluorescence (Ibrahim et al., 2010). Furthermore, t-tubule alteration is not always observed in heart failure, while the localized drop out in excitation–contraction coupling (ECC) efficacy apparently caused by t-tubule remodeling can be explained by the altered action potential waveform characterized by the reduced transient outward current (Bers, 2006; Harris et al., 2005).

An alternative approach to study the functional impact of t-tubules is numerical simulation, with which we can perform *in silico* experiments under totally controlled conditions. The crucial

\* Corresponding author. Tel.: +81 3 5841 8393; fax: +81 3 5841 6376.  
E-mail address: [sugiura@k.u-tokyo.ac.jp](mailto:sugiura@k.u-tokyo.ac.jp) (S. Sugiura).



part of the modeling of cardiac myocytes is the representation of the calcium-induced calcium release (CICR) mechanism. Until recently, the majority of studies used the ‘common pool model’ (Stern, 1992) in which all  $\text{Ca}^{2+}$  currents are mediated by the L-type  $\text{Ca}^{2+}$  channel (LCC) and the release flux from the SR flow into a common compartment, and the  $\text{Ca}^{2+}$  concentration in this compartment controls the activity of the SR  $\text{Ca}^{2+}$  release channel (ryanodine receptor: RyR). However, as this modeling strategy cannot reproduce the graded  $\text{Ca}^{2+}$  release, alternative formulations have been devised. For example, Greenstein et al. (2006) proposed a local control model in which simulated the gating of individual LCCs and RyRs in dyadic space to successfully reproduce the graded  $\text{Ca}^{2+}$  release. Nevertheless, both modeling approaches treat the subcellular spaces as a lumped compartment and ignore geometrical factors, and as such are unsuitable for examining the effect of structural changes in t-tubules. Three-dimensional (3D) models of cardiac myocytes studying the impact of 3D t-tubules on electrophysiology and 3D  $\text{Ca}^{2+}$  dynamics have also been reported (Cheng et al., 2010; Lukyanenko et al., 2009; Yu et al., 2011). However, although these models reproduce either a simple or realistic shape of t-tubule structure, other subcellular components are not explicitly modeled and the diffusion of  $\text{Ca}^{2+}$  is calculated in the homogeneous cytosolic space assuming a uniform distribution of troponin C throughout the cytosol.

Thus, as yet there are no simulation models that integrate the electrophysiology and contraction in a detailed 3D structure to examine the functional impact of t-tubule structure in health and diseased states. In the present study, we extended our previous system (Okada et al., 2005) to develop a finite element model of cardiomyocyte integrating electrophysiology,  $\text{Ca}^{2+}$  dynamics, and contractile process with detailed subcellular structures to evaluate the impact of the spatial arrangement of t-tubules in the signal transduction involved in ECC. The simulation results reproduced both the propagation of  $\text{Ca}^{2+}$  signals and the contractile behavior for both normal and detubulated myocytes previously reported in experimental studies. Furthermore, the detailed information provided on  $\text{Ca}^{2+}$  concentration, stress, and sarcomere strain beyond the limit of experimental approach demonstrated not only the importance of t-tubules in contractile function but also the utility of this model for studying cardiac mechanics.

## 2. Methods

### 2.1. 3D finite element model of the myocyte

The structure of the 3D finite element model of myocytes is shown in Fig. 1C–E. Ion channels, pumps, and exchangers are distributed in surface sarcolemma and t-tubules with specific densities, as previously reported for guinea pig ventricular myocyte (Pasek et al., 2008). Mitochondria were modeled as a  $\text{Ca}^{2+}$  sink, although energy metabolism was not incorporated in this study. To reduce computational costs the segment containing three myofibrils of one sarcomere length was modeled together with the adjacent cell membrane and organelle (2816 nodes and 2107 elements). The rationale behind this modeling strategy was the longitudinal periodicity and axial symmetry of the myocyte. Subcellular components including the mitochondria, myofibril (A-zone, I-zone, and M-line), junctional and network sarcoplasmic reticulum (JSR and NSR respectively), cell membrane, and t-tubules were located at the appropriate nodes to reproduce the anatomical structure and occupy the relative volume (Aliev et al., 2002; Bers, 2001; Chen-Izu et al., 2006; Cortassa et al., 2006). The function of each subcellular component was primarily based

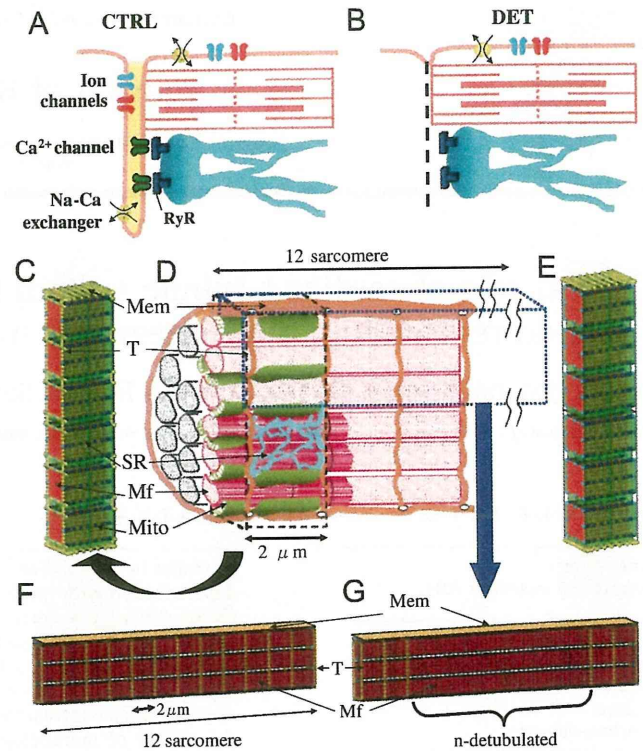


**Fig. 1.** (A) Control model (CTRL) with normal t-tubule structure. (B) Detubulated model (DET) with orphan ryanodine receptor. (C–E) Schematic diagram of the 3D cardiomyocyte model. (D) Six myofibrils of one sarcomere length were modeled in finite element mesh with subcellular structures (C, CTRL; E, DET). Ion channels and exchangers are distributed over the t-tubules and sarcolemma. Mem: sarcolemma, Mf: myofibril, Mito: mitochondria, SR: sarcoplasmic reticulum, T: t-tubule. (F) Twelve sarcomere mesh with normal t-tubule structure. (G) Twelve sarcomere mesh with t-tubule deleted in the mid n-sarcomeres.

on the previously proposed mathematical formulation for guinea pig ventricular cardiomyocyte (Cortassa et al., 2006). Additionally, to investigate the effect of regional disorganization of the t-tubule system, we created larger models consisting of three myofibrils of 12-sarcomere length (Fig. 1F and G). In these cases, to save the computational cost, coarse meshes were used and half of the model (6 sarcomere length) was calculated considering its symmetry. The model consisted of 4340 nodes and 3420 elements. The reaction–diffusion fields for  $\text{Ca}^{2+}$  were defined in the cytosolic space, as follows:

$$\frac{d[\text{Ca}^{2+}]_i}{dt} = \nabla \cdot (\mathbf{D} \nabla [\text{Ca}^{2+}]_i) + f_i([\text{Ca}^{2+}]_i) \quad (1)$$

where  $\mathbf{D}$  describes the diffusivity of  $\text{Ca}^{2+}$ ,  $[\text{Ca}^{2+}]_i$  is the concentration of  $\text{Ca}^{2+}$  at position  $i$ , and  $f_i([\text{Ca}^{2+}]_i)$  is the function describing the reaction of  $\text{Ca}^{2+}$  which corresponds to elementary processes of each subcellular components including mitochondria, JSR and so on, and which was defined appropriately for each node to reproduce the anatomical structure.

The diffusion coefficient for the longitudinal direction was estimated from an *in vitro* experiment (de Graaf et al., 2000) and set at  $D^{\text{Ca}} = 0.3$ , ( $\mu\text{m}^2/\text{ms}$ ). With regard to the coefficient in the transverse direction, we multiplied this value by 0.6265 based on *in vivo* cardiac myofibril results (Vendelin and Birkedal, 2008). Every node on the membrane and t-tubule permeates ions according to the local ion concentration and shares a membrane potential. As experimental data suggested that the whole cell membrane is electrically well coupled (Orchard and Brette, 2008), the membrane potential was treated as uniform throughout the



model. Ion channel distributions on peripheral and t-tubule membrane were defined as previously reported (Pasek et al., 2008) (see Supplemental Table 2). At the Ca<sup>2+</sup> release site the channel distribution is different from other regions of the t-tubule membrane, and only the L-type Ca<sup>2+</sup> channel (LCC) is clustered without other ion channels. Here, the LCC, JSR, subspace, and the local cytosolic space share a common node, but possess their own Ca<sup>2+</sup> concentrations for finite element analysis. Upon depolarization of the membrane potential triggered by stimulation current, LCC opens and the Ca<sup>2+</sup> current through the LCC (*I<sub>Ca</sub>*) flows into the subspace and activates ryanodine receptors (RyR) located on the JSR. This triggers Ca<sup>2+</sup> release from the JSR (*J<sub>rel</sub>*) into the subspace, and the released Ca<sup>2+</sup> moves to the cytosolic node to diffuse throughout the entire cytosol. Within the cytosolic space, Ca<sup>2+</sup> is either taken up by the Ca<sup>2+</sup> uniporter of the mitochondrial node, bound to troponin C on the thin filament, or is sequestered by Ca<sup>2+</sup> pump (SERCA2) on the NSR, before eventually being transported back to the JSR. Further details outlining the model can be found in Supplementary Material.

The contraction model developed by Negroni and Lascano (1996) was located at each point of the A-zone and generated force depending on the local Ca<sup>2+</sup> concentrations and sarcomere length. Using these force values as boundary conditions, the following mechanical equilibrium (2) and compressibility control condition (3) on variables (*u*, *λ*) were solved using the finite element method:

$$\int_V \left( 2 \frac{\partial W}{\partial \mathbf{C}} + \lambda \mathbf{J} \mathbf{C}^{-1} \right) : \delta \mathbf{E} dV + \int_{S_t} \tilde{\mathbf{t}}_b \cdot \delta \mathbf{u} dS = 0 \quad (2)$$

$$\int \delta \lambda \left( J - 1 \right) - \frac{2\lambda}{\kappa} dV = 0 \quad (3)$$

where *u* is displacement, *W* is strain energy potential, *C* is right Cauchy–Green deformation tensor, *E* is Green–Lagrange strain tensor, *J* is the square root of the determinant of *C*, *V* is analysis volume, *λ* is a Lagrange multiplier corresponding to  $-1/2$  of the pressure, *κ* is bulk modulus, *t<sub>b</sub>* is the stress boundary condition calculated from A-zone force generation, and *S<sub>t</sub>* is the surface where stress boundary condition is defined.

The cell was assumed as nearly incompressible hyperelastic material, with anisotropic constitutive equations for myofibril and isotropic constitutive equations of Mooney–Rivlin material for the other spaces previously reported (Okada et al., 2005). Full details of the mathematical modeling can be found online in Supplementary Material.

### 2.2. Detubulated myocyte models

The detubulated model (DET) was created by removing the t-tubules from the control model (CTRL) (Fig. 1A) along with the Ca<sup>2+</sup> channels, Na<sup>+</sup>–Ca<sup>2+</sup> exchangers, and other channels distributed in it. As a result, the Ca<sup>2+</sup> release channels (RyR) on the SR were left as orphan RyR (Fig. 1B). To analyze the effect of regional disorganization of the t-tubule system, we created two regionally detubulated models with either a large (8 sarcomere-length; DET8) or small (4 sarcomere-length; DET4) detubulated region, and compared them with the non-detubulated control myocyte model (Fig. 1F and G). We also compared the models in which half of the t-tubules were removed homogeneously (every other transverse tubule was deleted; homogenous model) or by deletion of the middle six t-tubules as a cluster (clustered model).

### 2.3. Simulating the adrenergic stimulation

In CTRL and DET models, the influences of adrenergic stimulation were simulated by up-regulation of L-type Ca<sup>2+</sup> channel current by 50%, lowering the threshold [Ca<sup>2+</sup>] level for Ca<sup>2+</sup> release from RyR by 20%, and tripling the maximum velocity of SR Ca<sup>2+</sup> pump, as previously reported (Brette et al., 2005, 2004). We also simulated a case in which only the L-type Ca<sup>2+</sup> current was up-regulated (Harris et al., 2005).

### 2.4. Computation

All the program codes (including solver and finite element integration) were written in-house using Fortran language, and the computation was performed using an Intel Xeon CPU (3.2 GHz).

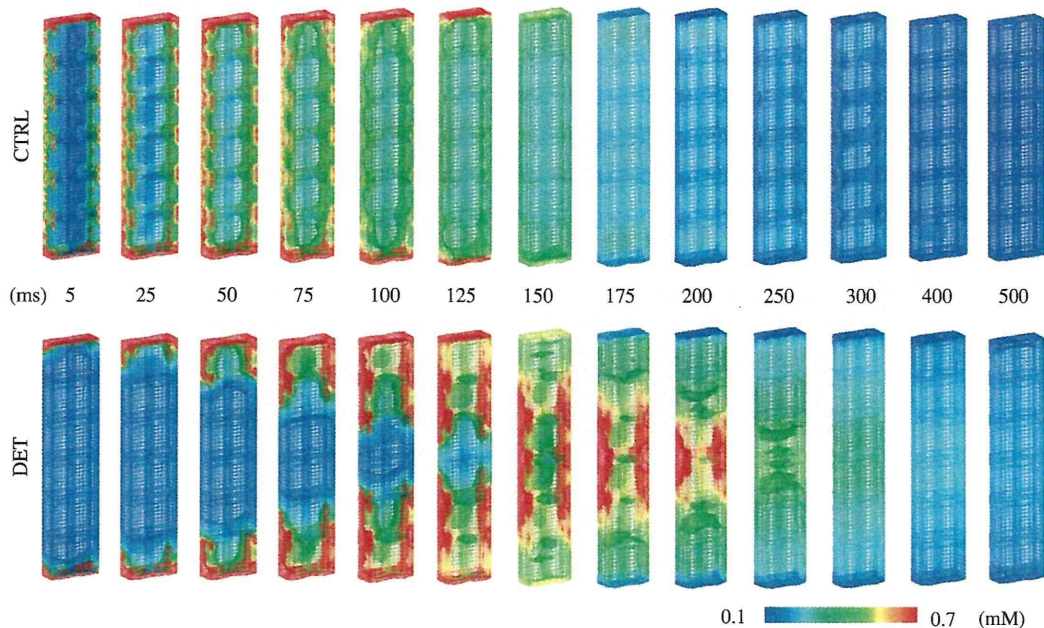


Fig. 2. Time lapse images of Ca<sup>2+</sup> propagation in control (CTRL) and detubulated (DET) myocyte models under unloaded conditions. Ca<sup>2+</sup> concentrations in the laterally arranged six sarcomeres are shown in color-coding indicated below. The numbers in the middle indicates the time (msec) after the stimulation.

### 3. Results

#### 3.1. $Ca^{2+}$ propagation and contraction in detubulated myocyte

The  $Ca^{2+}$  propagation and unloaded contraction of control and detubulated myocyte models in time-lapse images are shown in Fig. 2 (see also Supplemental Movie 1). In CTRL,  $[Ca^{2+}]$  increased simultaneously at the surface membrane and  $Ca^{2+}$  release sites distributed along the t-tubules, and rapidly propagated towards the A-line region. Consequently, all the sarcomeres in the model contracted synchronously. By contrast,  $[Ca^{2+}]$  in DET was initiated only at the surface membrane and propagated slowly to the center of the cell, resulting in slow and asynchronous contraction.

Supplementary material related to this article can be found online at doi:10.1016/j.jbiomech.2011.11.022.

Next, for comparison with the experimentally observed transverse line scan using confocal microscopy, we simulated isometric

contraction, and sampled and plotted the  $[Ca^{2+}]$  on the line running transversely along the t-tubules after the onset of excitation, as well as the local  $Ca^{2+}$  transients sampled at the sub-sarcolemma (SS) and core (CC) regions (Fig. 3A and B). The regularly spaced bright spots in these figures correspond to the  $Ca^{2+}$  release sites. There was a significant delay in local  $Ca^{2+}$  transients in the core region of DET compared with CTRL, and both the time to peak and the end of the whole-cell  $Ca^{2+}$  transient, averaged over the entire region, was significantly delayed compared with CTRL (black lines in the bottom panels). The propagation velocity of  $Ca^{2+}$  transients was  $31 \mu\text{m/s}$ , comparable to those observed experimentally ( $48.4 \pm 5.2 \mu\text{m/s}$ ; Yang et al. (2002)). Upon adrenergic stimulation, the amplitude of the  $Ca^{2+}$  transient increased and its duration decreased in CTRL (Fig. 3C). In the detubulated myocyte the lag between the periphery and the core was reduced (Fig. 3D), such that the whole-cell  $Ca^{2+}$  transient resembled that of the control (blue lines in the bottom panels). For validation, we compared these results with the

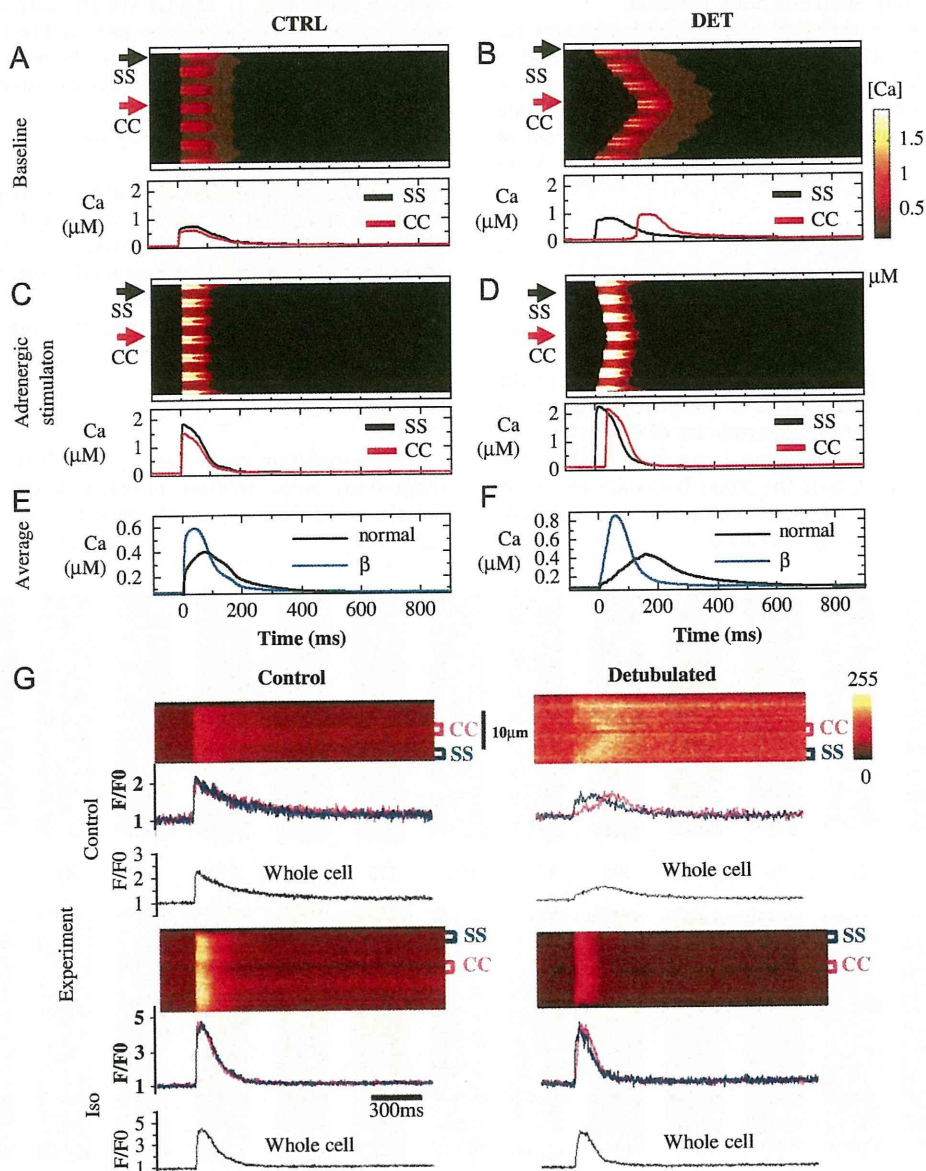


**Fig. 3.** Simulated transverse line scans of control (CTRL) model (A and C) and detubulated (DET) model (B and D) under control conditions (A and B) and under beta adrenergic stimulation (C and D) of isometric contraction. Each panel shows a line scan image of  $Ca^{2+}$  concentration with time courses of the local  $Ca^{2+}$  concentration sampled at the CC and SS (attached below). The bottom panels compare the whole cell averaged  $Ca^{2+}$  transients of A vs. C (in E) and B vs. D (in F). G) Experimental data of line scans and traces of local and averaged  $Ca^{2+}$  transients from Brette et al. (2004) are provided for comparison by copyright permission of Elsevier.



experimental observations of Brett et al. (2004) (Fig. 3G). Our simulation model reproduced the effect of detubulation under both baseline and adrenergic stimulation. On the other hand, when only the  $I_{Ca}$  was up-regulated, the re-synchronization effect was minimal and a significant delay in the local  $Ca^{2+}$  transient in the cell center remained. Propagations in the DET model under baseline (without adrenergic stimulation), up-regulation of  $I_{Ca}$ , and  $\beta$ -adrenergic stimulation are shown in Fig. 4. For baseline,  $I_{Ca}$  up-regulation, and  $\beta$ -adrenergic stimulation, propagation times were 150, 115, and 35 ms, respectively, and propagation velocities were 31, 40, and 133  $\mu\text{m}/\text{sec}$ , respectively.

We also examined the role of  $Na^+-Ca^{2+}$  exchanger (NCX) current distributed in t-tubules (Pasek et al., 2008) by comparing the averaged  $Ca^{2+}$  transients (Fig. 5A), L-type  $Ca^{2+}$  channel (Fig. 5B), and NCX (Fig. 5C) currents between the CTRL and the DET models. The total amounts flowing in and out of the model were compared for the currents. While the  $Ca^{2+}$  transient of the CTRL model exhibited a sharp rise triggered by the L-type  $Ca^{2+}$  channel current, the transient of the DET model triggered by diffuse  $Ca^{2+}$  increased slowly to its peak. After the peak, the  $Ca^{2+}$  transient of the DET model remained elevated. In the DET model, both the L-type  $Ca^{2+}$  channel current and the NCX current were significantly decreased compared with the control model, reflecting the localization of these currents in the t-tubules. These differences in currents contributed to the slow decay in the DET model, although the decay phase of the  $Ca^{2+}$  transient was dominated by the SR  $Ca^{2+}$  pump for both the CTRL and DET models.

### 3.2. Propagation of $Ca^{2+}$ is influenced by the contraction mode

Next, we compared transverse line scans of the  $Ca^{2+}$  signals under different loading conditions (Fig. 6). For the isotonic contraction, afterload was set at 25% of the maximum isometric force. As the afterload was reduced (A: isometric  $\rightarrow$  B: isotonic  $\rightarrow$  C: unloaded), shortening of the myocyte increased the cell width. Although the initial propagation speed was similar ( $\sim 30 \mu\text{m}/\text{s}$ ), the resultant widening of the space between the adjacent  $Ca^{2+}$  release sites caused a progressive delay in  $Ca^{2+}$  propagation ( $\sim 20 \mu\text{m}/\text{s}$ ), and the propagation was finally terminated under

the unloaded condition (Fig. 6C). A similar phenomenon was reported in the experimental study by Yang et al. (2002) (Fig. 6D).

### 3.3. Regional loss of t-tubules

The effects of regional detubulation on  $Ca^{2+}$  transient and contraction were examined using the 12-sarcomere model under isometric conditions (Fig. 7A). In contrast to the control myocyte showing synchronized  $Ca^{2+}$  transient and contraction, slow propagation of  $Ca^{2+}$  in the detubulated region progressively delayed the completion of contraction as the detubulated region became increased (Fig. 7A and Supplemental Movie 2). The amplitude and timing of the peak isometric force were also decreased and delayed, respectively, depending on the size of the detubulated region (Fig. 7B). To further analyze the contractile dysfunction of the detubulated myocyte, we examined the  $Ca^{2+}$  transient, sarcomere length, and developed force at each sarcomere (Fig. 8). The presentation mimicking the longitudinal line scan mode clearly demonstrated a progressive delay of  $Ca^{2+}$  propagation toward the center of the detubulated region (Fig. 8 top panels). Although the total muscle length was made isometric, asynchrony of the local  $Ca^{2+}$  transient in the detubulated models induced the internal shortening of the early-activated sarcomere and lengthening of the resting sarcomere (Fig. 8, middle panels). In particular, the large internal shortening observed in the DET8 model with the large detubulated region is the likely cause of the greater depression in initial rise of isometric force (Fig. 7B), via inhibition of development of force locally (Fig. 8 bottom panels). To investigate the effect of the size of individual detubulation, we also compared the homogeneous model and the clustered model that both had the same number of t-tubules. The homogeneous model showed no variation in sarcomere length, and the force developed smoothly, similar to the control myocyte without detubulation (Fig. 9). Internal shortening in the clustered model caused the depression of force development in the initial phase (Fig. 7C), and may also have induced a deleterious effect. In addition, although energy metabolism was not considered in this simulation, internal shortening is expected to reduce the contractile efficiency by wasting energy according to the Fenn effect.

Supplementary material related to this article can be found online at doi:10.1016/j.jbiomech.2011.11.022.

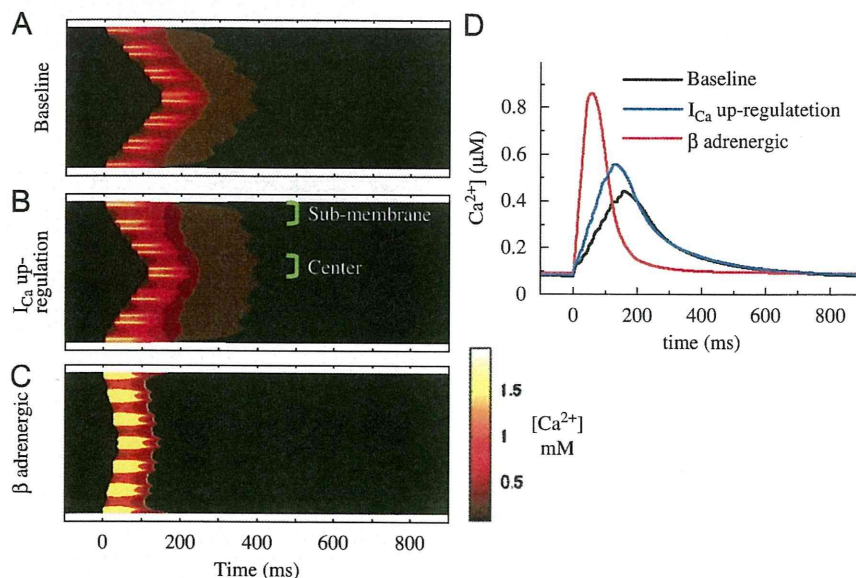


Fig. 4. Simulated transverse line scans and averaged  $Ca^{2+}$  transients of the detubulated model during the isometric contraction under baseline (A and D, black line),  $I_{Ca}$  up-regulation (B and D, blue line), and  $\beta$ -adrenergic (C and D, red line) conditions.



## 4. Discussion

### 4.1. 3D model of cardiomyocyte

In the present study, we extended our previous 3D cardiomyocyte model to incorporate ion currents distributed heterogeneously in the surface membrane and the t-tubule system to examine the impact of the t-tubule system on cardiac function. We adopted the sarcomere model of Negroni and Lascano (1996) for cardiac contraction. Although this simple model is not capable of reproducing the cooperative activation of actin-myosin interactions, we previously reported its robustness and compatibility with the FEM model (Okada et al., 2005; Watanabe et al., 2004). These complex models can reproduce various phenomena including cooperativity, quick-stretch, and release, but may require significant computational cost. The models of electrical activity by Cortassa et al. (2006) do not differ significantly from the model by Rudy (Livshitz and Rudy, 2007), but allow us to extend the model to include metabolic processes in future studies. However, as this model is a lumped parameter model, the distributions of ion channels in the t-tubule system and the volume fraction of the sub-compartments require adjustment for the current 3D model.

In the detubulated model,  $\text{Ca}^{2+}$  transients initiated at the peripheral membrane by depolarization propagate to the center of the cell slowly by a series of reaction diffusion processes (CICR). As a result, the  $\text{Ca}^{2+}$  transient averaged over the entire region showed a delay in time to peak and a slow decay. Slow decay was also observed in local  $\text{Ca}^{2+}$  transients due to the loss of t-tubular Na-Ca exchange current, as suggested experimentally (Kawai et al., 1999; Pasek et al., 2008; Yang et al., 2002). In addition, under adrenergic stimulation, the detubulated model showed faster  $\text{Ca}^{2+}$  propagation and the synchronization of the  $\text{Ca}^{2+}$  transient was restored. The lower threshold  $[\text{Ca}^{2+}]$  level for  $\text{Ca}^{2+}$  release and the larger  $\text{Ca}^{2+}$  release flux through up-regulation of LCC and SR (up-regulation of SR  $\text{Ca}^{2+}$  pump resulted in higher content and larger release) accelerated the CICR and the reaction-diffusion processes. This synchronizing effect of beta

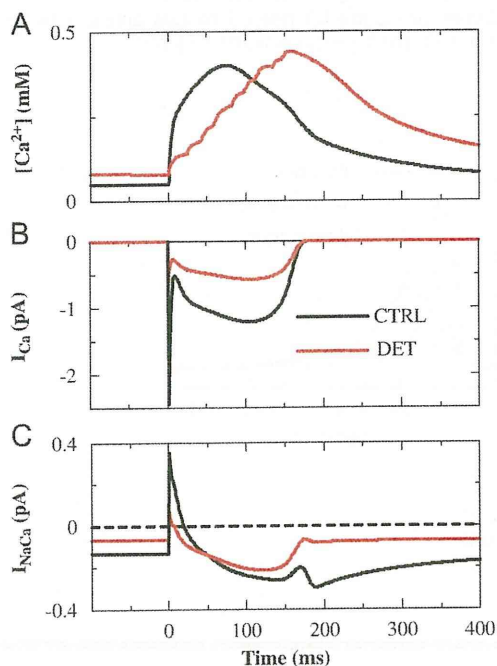


**Fig. 5.**  $\text{Ca}^{2+}$  transients and currents in CTRL (black line) and DET (red line) models under isometric condition. (A)  $\text{Ca}^{2+}$  transients averaged over the sarcomere. (B) L-type  $\text{Ca}^{2+}$  channel current. (C)  $\text{Na}^{+}$ - $\text{Ca}^{2+}$  exchanger current.

adrenergic stimulation on detubulated cells was also observed in experimental studies (Brette et al., 2004; Smyrniak et al., 2010). In contrast to our simulation results, Harris et al. (2005) was able to recover synchronous  $\text{Ca}^{2+}$  release in failing feline myocytes only by increasing  $I_{\text{Ca}}$  induced by the normalization of action potential. However, although the authors did not examine the t-tubule morphology in their failing myocytes, they show a spotty  $\text{Ca}^{2+}$  release pattern suggesting that a large area of couplon loss did not take place in their preparations. Considering our simulation result with the small detubulated region (DET4 or homogeneous model), we speculate that if the area of detubulation is small, only the increase in  $I_{\text{Ca}}$  could allow recovery of the normal cardiomyocyte E-C coupling function, while if the area of detubulation is large, the recovery may not be possible even with multiple compensatory mechanisms.

### 4.2. Impact of t-tubule disorganization on cardiac dysfunction of the diseased heart

In cardiomyocytes isolated from diseased hearts, t-tubules are lost heterogeneously and the area of disorganization increases progressively (Cannell et al., 2006; Heinzel et al., 2008; Louch

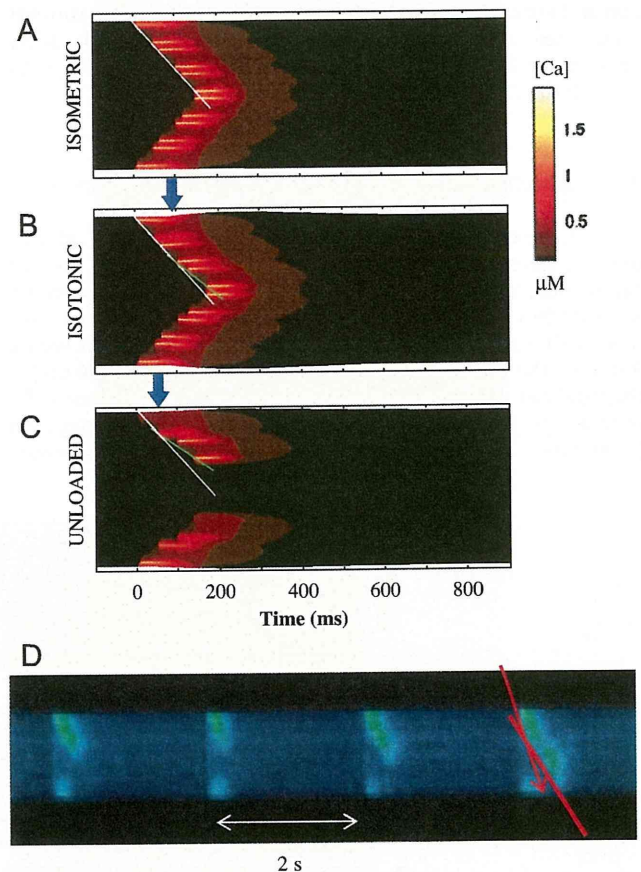


**Fig. 6.** Transverse line-scan images of detubulated (DET) model under different contraction modes. (A) Isometric contraction. (B) Isotonic contraction. (C) Unloaded contraction. While a single tangential line (white line) was well fit to the  $\text{Ca}^{2+}$  propagation in A, additional lines (green) were required in B and C due to the reduction of propagation velocity in the core region. Propagation velocity calculated from the slope of the tangential lines were similar in all cases at the initial part (white line:  $31 \mu\text{m/s}$ ), but decreased in B ( $21 \mu\text{m/s}$ ) and C ( $18 \mu\text{m/s}$ ), both calculated from the slope of the green lines. Blue arrows indicate the initiation of widening. (D) Experimental transverse line-scan image of detubulated myocyte demonstrating incomplete propagation of  $\text{Ca}^{2+}$ . Two tangential lines were fit, similar to above (reproduced from Yang et al. (2002) by copyright permission of the American Heart Association).